Ore Geology Reviews 95 (2018) 1008–1027

Contents lists available at ScienceDirect

Ore Geology Reviews

journal homepage: www.elsevier.com/locate/oregeorev

The role of hydrothermal alteration in tungsten mineralization at the Dahutang tungsten deposit, South China

Yong Zhang[a,b,*], Jian-Feng Gao[c], Dongsheng Ma[a], Jiayong Pan[b]

[a] School of Earth Sciences and Engineering, Nanjing University, Nanjing 210046, China
[b] School of Earth Sciences, East China University of Technology, Nanchang 330013, China
[c] State Key Laboratory of Ore Deposit Geochemistry, Institute of Geochemistry, Chinese Academy of Sciences, Guiyang 550081, China

ARTICLE INFO

Keywords:
Mineralogy
Geochemistry
Hydrothermal alteration
Tungsten mineralization
Dahutang tungstendeposit
South China

ABSTRACT

The giant Dahutang tungsten deposit has total reserves of more than 1.31 Mt of WO_3 with a scheelite/wolframite ratio of ~1 and is mainly hosted by the Neoproterozoic Jiuling granodiorite batholith (~820 Ma). The deposit is characterized by four types of alteration, including biotite alteration, phyllic alteration, greisenization and silicification. Whole-rock geochemical analyses showed that the elements Ti, Ni, V, Sc, and Lu exhibited immobility during the four alteration processes. The mobile element geochemistry effectively differentiated among four distinct hydrothermal alteration styles. During the biotite mineralization, there were mass gains in Al_2O_3, Fe_2O_3, MnO, MgO, K_2O, P_2O_5, and W and depletions in SiO_2, CaO, and Na_2O. The phyllic alteration exhibited mass gains in SiO_2, Fe_2O_3, MgO, and W and depletions in CaO, Na_2O, and K_2O, but Al_2O_3, MnO, and P_2O_5 were immobile. The weak greisenization exhibited mass gains in SiO_2, Fe_2O_3, K_2O, P_2O_5 and W and depletions in Na_2O, MgO, and CaO, whereas Al_2O_3 and MnO remained immobile. The silicification exhibited mass gains in SiO_2 and W and depletions in Al_2O_3, Fe_2O_3, MgO, CaO, Na_2O, and K_2O, but MnO exhibited immobility. These alterations were related to at least three major hydrothermal fluid systems. Firstly, a hydrothermal fluid caused biotitization zones and Fe + Mn ± W mineralization (mostly biotite) at temperatures ranging from 560 to 450 °C, and the magmatic hydrothermal fluids were derived from the Jurassic porphyritic biotite granite (~150 Ma) and characterized by alkaline, oxidized, moderate-pressure, and low-salinity features. Secondly, a hydrothermal fluid was formed by the mixing of magmatic fluid with meteoric water and was responsible for the phyllic/weak greisenization alteration zones at temperatures ranging from 440 to 450 °C and characterized by alkaline, weakly oxidized, moderate-pressure, and low-salinity features. Thirdly, a hydrothermal fluid caused greisenization and silicification zones at temperatures ranging from 440 to 160 °C, which were characterized by acidic, reduced, high-pressure, and moderate- to low-salinity features, derived from the Cretaceous fine-grained biotite granite (~144 Ma), and associated with the main W mineralization at Dahutang.

The characteristics of Fe-enriched biotite in the biotitized and greisenized rock – decreasing temperature, high pressure, and high $\log(fH_2O/fHCl)$ – could facilitate the formation of scheelite deposits, but the high F suppressed it. The decreasing temperature and $f(O_2)$ and the Fe-Mn released from biotite contributed to the formation and precipitation of wolframite. During alkaline alteration, biotite and apatite acted as storage places for Fe-Mn and Ca, which were subsequently released by acidic alteration to form scheelite and wolframite. There was no enough Ca was released from biotitized rock for the acidic alteration to provide the WO_4^{2-} to form scheelite. Meanwhile, Fe was added, and Mn was released to form the scheelite + wolframite deposit. Based on all the results, we have developed a genetic model for tungsten mineralization including superimposed alteration processes (alkaline overprinted by acidic alteration), which led to the gain and loss of elements, and corresponding to two magmatic events, the Jurassic porphyritic biotite granite and the Cretaceous fine-grained biotite granite. The superposition of alterations played an important role in the mineralization of the Dahutang giant tungsten deposit.

* Corresponding author at: School of Earth Sciences and Engineering, Nanjing University, Nanjing 210046, China.
E-mail address: zhycy2004@163.com (Y. Zhang).

https://doi.org/10.1016/j.oregeorev.2018.04.006
Received 6 December 2017; Received in revised form 2 April 2018; Accepted 4 April 2018
Available online 05 April 2018

1. Introduction

Hydrothermal mineralization is commonly associated with metasomatic alteration. Particularly in a granite-related mineralization system, alteration is very important for the transportation and deposition of ore metals (Aliyari et al., 2014; Heinrich and Candela, 2014; Li et al., 2013; Pirajno, 2009; Putnis, 2009). Each ore system has a distinctive alteration process, and thus, different types of alteration are related to different types of mineralization. For example, porphyry copper deposits (PCD) are commonly characterized by several representative alteration types (potassic, prophylitic, phyllic, and argillic), which are linked to porphyry Cu ± Au ± Mo mineralization, subepithermal vein-type Zn-Cu-Pb-Ag ± Au mineralization, high-sulfidation lode Cu-Au ± Ag mineralization, and intermediate-sulfidation epithermal Au-Ag mineralization, respectively (Gustafson and Hunt, 1975; Lowell and Guilbert, 1970; Sillitoe, 1997; Sillitoe, 2010). PCD are dominated by fluid-rock interactions to form large accumulations of sulfur, and the type of alteration constrains the different ore types. The processes of porphyry hydrothermal alteration and mineralization are well-understood (Cooke et al., 2014; Corbett and Leach, 1998; Harris and Golding, 2002; Kusakabe, 1984; Kusakabe et al., 1990; Watanabe and Hedenquist, 2001; Wolfe et al., 1996). However, research on the relationship between tungsten mineralization and the relevant alteration is comparatively rare. Granite-related tungsten mineralization is characterized by various types of alteration, including potassic alteration, biotitization, greisenization and silicification (Hu et al., 2004; Mao et al., 1996; Pirajno, 2013a; Soloviev and Kryazhev, 2016; Wang et al., 2016). Tungsten mineralization is commonly characterized by wolframite or scheelite in individual deposits, which have different origins. Wolframite mineralization invariably accompanies greisen, while scheelite mineralization is mostly associated with skarnization (Feng et al., 2011; Mao et al., 1996; Raith and Prochaska, 1995; Raith and Stein, 2000; Soloviev and Kryazhev, 2016; Wang et al., 2016; (Zhao and Zhou, 2018; Zhao et al., 2018). However, the discovery of the giant Dahutang W deposit, containing > 1.31 Mt of WO_3, challenges this pattern. In this deposit, there are nearly equal amounts of scheelite and wolframite (Liu et al., 2016)[1]. The tungsten mineralization is associated with extensive alkali alteration overprinted (superposed) locally by greisenization and silicification. These types of alteration are spatially related to the tungsten mineralization, while their genetic relationship with the mineralization is not clear. Thus, this lack of clarity has impeded our understanding of the delicate alteration process and ore genesis of this deposit.

The Dahutang tungsten ore is spatially related to the roof of some felsic intrusions, including a Jurassic porphyritic biotite granite pluton and a Cretaceous fine-grained biotite granite pluton (Zhao et al., 2017). Drill cores show that the tungsten mineralization occurs at the contact between the Late Mesozoic granite stocks (the third phase ~150 Ma) (Mao et al., 2015; Ye et al., 2016; Zhang et al., 2016) and the Jiuling Neoproterozoic (~820 Ma) granodiorite batholith (Li et al., 2003; Zhong et al., 2005) or the Neoproterozoic slate. The majority of the well-known work on the Dahutang tungsten deposit emphasizes the petrogenetic and metallogenic geochronology to obtain many important and meaningful research results (e.g., Han et al., 2016; Huang and Jiang, 2014; Jiang et al., 2015; Mao et al., 2013; Mao et al., 2015; Ruan et al., 2015; Wei et al., 2017; Zhang et al., 2016). However, much of the basic geology remains to be examined, such as the principal variables in alteration, the ore-forming temperature and the processes related to fluid composition.

In this study, we describe in detail the geology of the deposit and the features of alteration of the Dahutang tungsten deposit: (a) We examine the detailed gains/losses in ore-forming elements during the alteration processes from the petrography and geochemistry of fresh and altered specimens. (b) We examine the genetic connections of different types of alteration by using biotite geochemistry. All these results are used to develop a genetic model for the Dahutang tungsten deposit.

2. Regional geology

2.1. The Jiangnan orogenic belt

The Jiangnan orogenic belt is the northeastern boundary between the Cathaysia and the Yangtze Block (Li et al., 2009; Shu, 2012; Shu et al., 1995) (Fig. 1). This orogenic belt is rich in mineral resources and has a wide diversity of deposit types. This region has undergone multiple phases of tectonic, magmatic and metallogenic events.

The Jiangnan orogenic belt experienced multiple orogenies from the Middle Proterozoic to the Cretaceous (Fig. 1), such as the amalgamation of the Yangtze Craton with the Cathaysia Block approximately 860–800 Ma (Wang et al., 2012; Wang et al., 2007; Zhong et al., 2005; Zhou et al., 2002), a syncollisional volcanic arc that developed from immature continental crust during the Neoproterozoic (Xiang et al., 2012; Zhao et al., 2011), and a series of thrusted nappe structures that trend nearly E-W and NE and contain an ophiolitic-type mélange and high-pressure metamorphic rocks (Pirajno, 2013b). During the Early Paleozoic, an orogenic event occurred from 465–430 Ma, leading to the formation of nearly E-W-striking top-to-the north thrusting (Xu et al., 2015). During the Early Mesozoic, intracontinental orogenies resulted in compression from 245–225 Ma and in collapse and magmatism from 225–215 Ma, forming N- to NE-striking fold and thrust structures and granites (Chu et al., 2015; Xu et al., 2015). During the Early Jurassic, an intracontinental orogen related to the low-angle subduction of an oceanic plate under the South China Block occurred, which led to a subsequent series of Late Mesozoic intracontinental tectonic processes and magmatic activity (Xu et al., 2009). During the Late Cretaceous, in response to a tectonic transition, there was a change from a continental margin environment to a lithospheric extensional regime (Liu et al., 2012), and the change from the compressive tectonic regime to the extensional regime began in the Early Cretaceous (Zhang et al., 2012).

The Jiangnan orogenic belt is composed mainly of Proterozoic low-grade sedimentary rocks and igneous rocks (the Pingshui, Xingzi, Shuangqiaoshan, Banxi, Lengjiaxi, Sibao, Fanjingshan, and Xiajiang groups from east to west). The Pingshui Group is a sequence of weakly deformed, low-grade metamorphosed marine volcanic lavas, volcaniclastic rocks and sedimentary pyroclastic rocks; in the southern part of this orogenic belt, the U-Pb age of detrital zircons is ~828 Ma (Han et al., 2015). The Xingzi Group is composed mainly of low-pressure, high-temperature gneisses and mica schists; in the middle part of this orogenic belt, the U-Pb dating of zircons from spilite and rhyolite yields ~830 Ma (Gao et al., 2012b; Guan et al., 2010). The Shuangqiaoshan Group is an important stratigraphic unit in this belt and consists of Neoproterozoic low-grade metamorphosed sedimentary strata; the U-Pb dating of zircons from the tuff is ~825 Ma (Gao et al., 2012b; Gao et al., 2008; Wang et al., 2008; Zhou et al., 2012). The Lengjiaxi Group comprises low-grade rocks; in the western part of this belt, the U-Pb dating of zircons from tuff yields ~822 Ma (Gao et al., 2011; Gao et al., 2012a; Meng et al., 2013). The Banxi Group comprises low-grade rocks; in the western part of this belt, the U-Pb dating of zircons from bentonite yields ~802 Ma (Gao et al., 2011). The Sibao Group is composed of low-grade metamorphosed rocks; in the western part of this belt, the U-Pb dating of zircons from tuff yields ~841 Ma (Gao et al., 2010). In addition, the Fanjingshan (U-Pb dating of zircons from tuff yields ~840 Ma) and Xiajiang (U-Pb dating of detrital zircons yields ~813 Ma) groups comprise low-grade rocks in the western part of this belt (Gao et al., 2014). All the Proterozoic low-grade sedimentary strata are enriched in ore metals (W, Sn, Mo, Bi, Pb, Zn, Sb, Ag, Au and others).

[1] Special mapping and technology application demonstration of the Dahutang tungsten monoblock exploration area. Written by Nanqing Liu, Xinkui Xiang, Hanming Ye, Yong Zhang, Gangle Zan, et al., 2016.

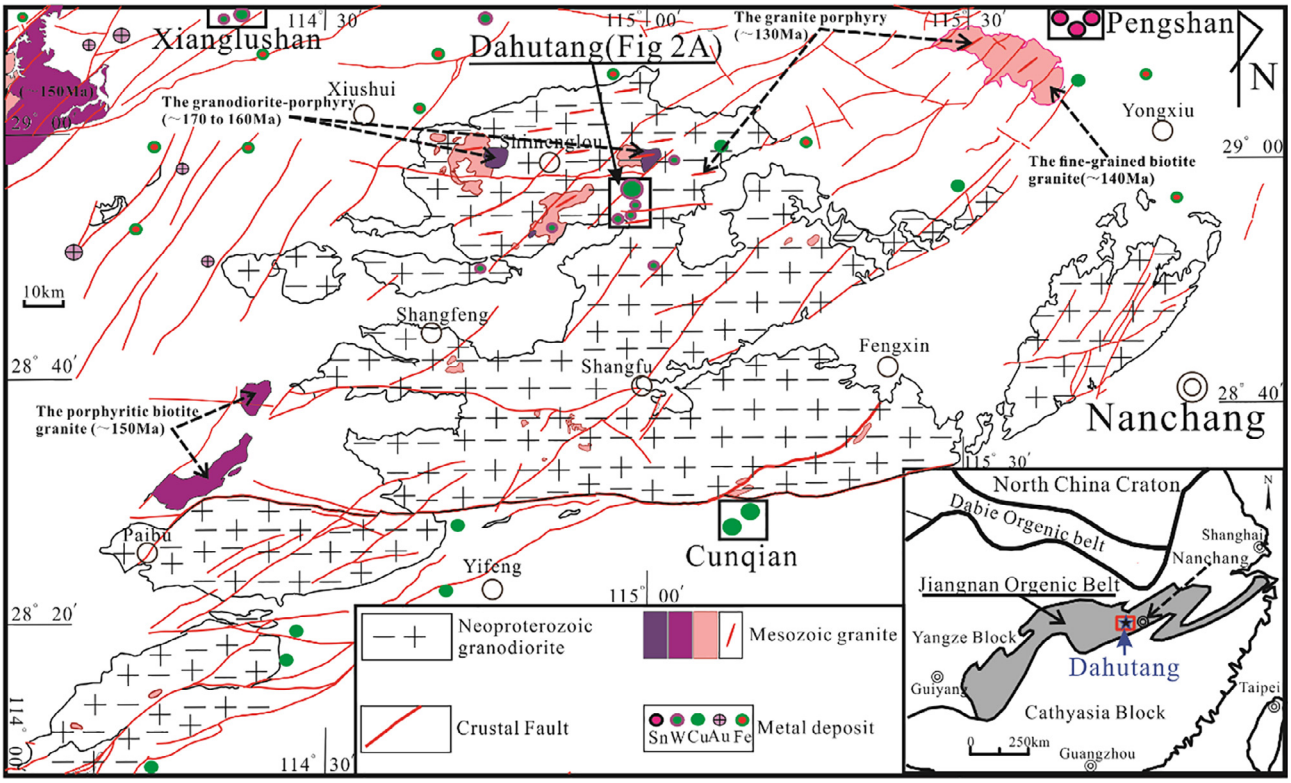

Fig. 1. Geological sketch map of the Jiuling granitic complex (after Li et al., 2003; Wang et al., 2008, Yang et al., 2004; Zhong et al., 2005).

Many porphyry deposits, epithermal deposits, skarn deposits, Kiruna-type deposits, metalliferous black shale-hosted deposits, granite-related tin-tungsten deposits, and hydrothermal gold deposits occur in the Jiangnan orogenic belt. These deposits are generally related to Triassic or Yanshanian (Jurassic to Cretaceous) magmatism associated with collision of the South China Continent and North China Cratons or with the westward subduction of the Paleo-Pacific Plate (Zaw et al., 2007; Zhao et al., 2017). There are many world-class W-Sn deposits in the belt, including Zhuxi (Chen et al., 2012; Liu et al., 2017), Dahutang (Xiang et al., 2012), Xianglushan (Xiong et al., 2015), and Penshan (Luo et al., 2010) (Fig. 1), making Jiangnan the largest W metallogenic prospective belt in the world.

2.2. The Jiuling batholith

The Neoproterozoic Jiuling granodioritic batholith is the largest granitoid complex in southeastern China, with an outcrop area greater than 2500 km^2 (Fig. 1). The batholith intruded the Shuangqiaoshan Group ~820 Ma (Fig. 1) (Li et al., 2003; Zhong et al., 2005).

The Jiuling batholith is composed mainly of biotite-rich, cordierite-bearing granodiorite. It has an anisomerous granitic texture and consists mainly of quartz, plagioclase, K-feldspar, biotite and muscovite with minor zircon, apatite, garnet, and ilmenite (Fig. 6a, b). The predominant textures include coarse-grained texture, porphyritic-like texture, and granoblastic texture. Subhedral to euhedral plagioclase is the most common phenocryst phase, and some of these crystals exceed 1–10 mm in length. The plagioclase phenocrysts often show normal or oscillatory zoning.

The Mesozoic granitic rocks in the study area are present as many small stocks that intruded both the Neoproterozoic granodiorite batholith and Precambrian strata (Mao et al., 2013) (Fig. 1).

The granodiorite-porphyry/porphyry consists of I-type granites formed from 170 to 160 Ma (Ding et al., 2005; Hu et al., 2015; Lou et al., 2005; Wang et al., 2004). The phenocrysts of the granodiorite-porphyry include mainly plagioclase, amphibole, and biotite with minor potassium feldspar and quartz. The matrix minerals are mainly cryptomerous plagioclase, amphibole, biotite, potassium feldspar, and quartz. The auxiliary minerals include magnetite, apatite, sphene, ilmenite, and pyrophyllite.

The porphyritic biotite granite, an S-type granite, formed approximately ~150 Ma (Huang and Jiang, 2014; Jia et al., 2015a; Li et al., 2014; Liu et al., 2008; Mao et al., 2015;Ye et al., 2016; Zhang et al., 2016). The porphyritic biotite granite has a porphyraceus texture. The phenocrysts are mainly quartz (2–3 mm), K-feldspar (1–4 mm), and plagioclase (2–3 mm). The matrix is macrocrystalline (0.1–1 mm) and composed of biotite, quartz, K-feldspar, plagioclase, and biotite.

Most of the fine-grained biotite granite, an S-type granite, formed approximately 144 Ma (Ding et al., 2005; Huang and Jiang, 2014; Jia et al., 2015b; Lou et al., 2005; Mao et al., 2015) and intruded the porphyritic biotite granite, although some have also intruded the Neoproterozoic granodiorite batholith. The fine-grained granite has a granitic texture and is composed mainly of plagioclase, K-feldspar, quartz, and biotite. Accessory minerals include pyrite, ilmenite, arsenopyrite, rutile, monazite, and spinel.

The granite porphyry is an S-type granite that formed ~130 Ma (Ding et al., 2005; Huang and Jiang, 2013, 2014; Lou et al., 2005). The granite porphyry intrudes both the fine-grained granite and porphyritic biotite granite. The granite porphyry is light gray and exhibits a porphyritic texture. The phenocrysts are euhedral quartz (1–3 mm) and K-feldspar (0.5–2 mm). The matrix mainly includes cryptomerous quartz and fine-grained muscovite.

3. Geology of the Dahutang deposit

The Dahutang deposit is composed of four segments, namely, *Shimensi*, *Dawutang*, *Shiweidong*, and *Kunshan* (see Fig. 2a and b). This deposit is situated in Wuning County of Jiangxi Province, approximately 120 km NW of Nanchang (Fig. 1). The Shuangqiaoshan Group is well-exposed south of the Dahutang deposit (Fig. 2a) and was intruded by the Jiuling granodiorite batholith, including both fine-grained

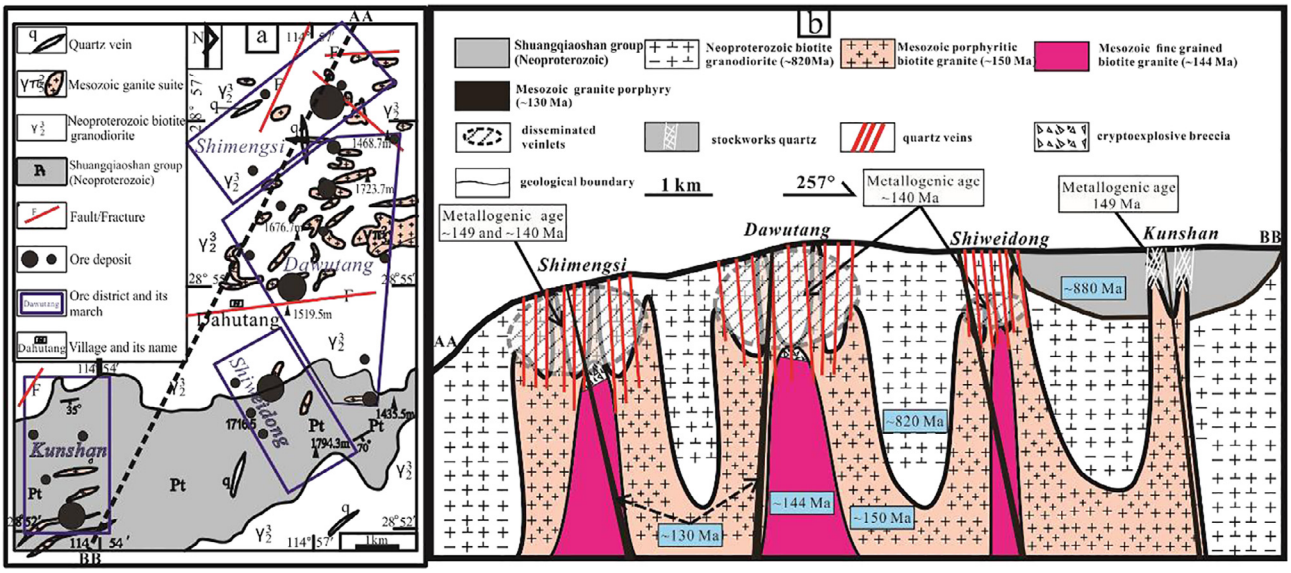

Fig. 2. Geological sketch map (a) and geological cross-section "AA-BB" (b) of the Dahutang tungsten deposit. a: Geological sketch map of the Dahutang tungsten deposit, which includes the four mines *Shimengsi*, *Dawutang*, *Shiweidong*, and *Kunshan* and their mining boundaries (modified from No. 916 Geological Team, Jiangxi Bureau of Geology, oral report, 2015). b: Geological cross-section through the four segments in the Dahutang tungsten deposit.

biotite granite and two-mica granite with calc-alkaline affinity (Fig. 2a). Both the Shuangqiaoshan Group and the Jiuling granitic batholith were intruded by Mesozoic granites, including the porphyritic biotite granite (151.7 ± 1.3 Ma to 147.4 ± 0.58 Ma) (Mao et al., 2015; Ye et al., 2016; Zhang et al., 2016), the fine-grained biotite granite (146.1 ± 0.64 to 144.7 ± 0.47) (Huang and Jiang, 2014; Jiang et al., 2015), and the granite porphyry/porphyry (~130.0 Ma) (Huang and Jiang, 2013, 2014).

The porphyritic biotite granite is gray to white (Fig. 1), with as much as 35–50% modal percent phenocrysts. The phenocrysts are quartz (~35 to 40%, 1–3 mm in diameter), K-feldspar (~35%, 0.5–4 mm in diameter), plagioclase (10–15%), and biotite (10%) in a fine-grained matrix. The matrix is composed of quartz, K-feldspar, plagioclase, and biotite. The phenocrysts often show corroded textures with jagged edges and sieve-like interiors. Accessory minerals include apatite, zircon, garnet, ilmenite, magnetite, monazite, epidote, tetrahedrite, and arsenopyrite.

The fine-grained biotite granite is composed of 20–25% plagioclase, 30–35% K-feldspar, 35–40% quartz, and ~7% biotite. The plagioclase crystals are typically 1.4–2.4 mm × 0.6–0.8 mm in size and subhedral in form, and they commonly exhibit polysynthetic twins, with less common Carlsbad–albite twins. Biotite flakes are mainly euhedral. Accessory minerals include pyrite, ilmenite, arsenopyrite, rutile, monazite, and zinc spinel.

The granite porphyry has phenocrysts accounting for 50–85% of the rock mass. They comprise euhedral quartz (30–35%, 1–3 mm in diameter), K-feldspar (40–45%, 0.5–2 mm in diameter and typically displaying Carlsbad twinning) and plagioclase (15–20%, mostly subhedral to euhedral in shape, 0.5 mm in diameter, and displaying polysynthetic twinning). The main accessory minerals are apatite, zircon, rutile, ilmenite, and magnetite. The porphyry has phenocrysts accounting for 20–50% of the rock mass. The phenocrysts are euhedral quartz, K-feldspar, and plagioclase that is mostly subhedral to euhedral and 0.5 mm in diameter and displays polysynthetic twinning. The main accessory minerals are apatite, rutile, ilmenite, magnetite, and pyrite. The granite porphyry and porphyry truncate all the tungsten mineralization, the porphyritic biotite granite, and the fine-grained biotite granite. This deposit had two main periods of mineralization.

The mineralization ages of the Dahutang tungsten deposit are mostly concentrated at 140 Ma and 150 Ma from the molybdenite Re-Os model age histogram (Zhang et al., 2017). Molybdenite from the *Shimengsi* segment has Re-Os isochron ages from 139.18 ± 0.97 Ma (Mao et al., 2013) to 143.7 ± 1.2 Ma (Feng et al., 2012) and 149.6 ± 1.2 Ma (Xiang et al., 2013). Molybdenite from the *Dawutang* segment has a Re-Os isochron age of 137.9 ± 2.0 Ma (Zhang et al., 2017). Molybdenite from the *Shiweidong* segment has a Re-Os isochron age of 140.9 ± 3.6 Ma (Feng et al., 2012). Molybdenite from the *Kunshan* segment has a Re-Os isochron age of 151.0 ± 1.3 Ma (Zhang et al., 2016). These mineralization ages correspond to the two phases of Cretaceous magmatism that produced the porphyritic biotite granite (~150 Ma) and the fine-grained biotite granite (~144 Ma) (Zhang et al., 2017).

The mineralization in the Dahutang tungsten deposit is characterized by (1) disseminated-/ veinlet-type tungsten mineralization in the Jiuling biotite granodiorite (~95% of the total reserve), which is associated with the roof of the porphyritic biotite granite stock (Fig. 2b, 3l); (2) cryptoexplosive breccia ores with the occurrence of wolframite, scheelite, chalcopyrite, and molybdenite (~4%) (Fig. 3f and i); and (3) quartz veins and stockworks of wolframite-scheelite (~1%) (Fig. 2b, 3a–h). The ratio of scheelite to wolframite is approximately 1, unlike the Nanling tungsten province (Liu et al., 2011) that contains carbonate-hosted scheelite- or wolframite-dominant deposits (Appel, 1994; Beran et al., 1985; Neinavaie et al., 1989; Plimer, 1994; Raith, 1991; Thalhammer et al., 1989).

Four alteration types have been recognized throughout the Dahutang alteration zone. I: Biotite alteration, characterized by two types of biotite, re-equilibrated and hydrothermal biotite, accompanied by mineralization (mostly a biotite ± wolframite ± apatite assemblage). II: Phyllic (fine-grained aggregate of muscovite (sericite) ± quartz) alteration with hydrothermal alteration immediately after the biotitization, with some sulfides deposited nearly since the beginning. III: Greisenization comprising muscovite ± quartz + wolframite + scheelite ± sulfide. IV: Silicification (hydrothermal quartz and quartz veins) that overprint the previous stages (Fig. 4).

The most intensely mineralized zone occurs within an 800 m-wide cone in the *Shimengsi* segment with reserves of more than 0.74 Mt WO_3 (Xiang et al., 2013), where the Jurassic porphyritic biotite granite is surrounded by granodiorite that forms a large biotitization + greisenization ± silicification alteration halo (Fig. 2b). Surrounding the semi-round circumnuclear intrusive roof of the porphyritic biotite granite, the cone has a radius of ~500 m and a vertical height of 250 m. The main tungsten mineralization is concentrated in

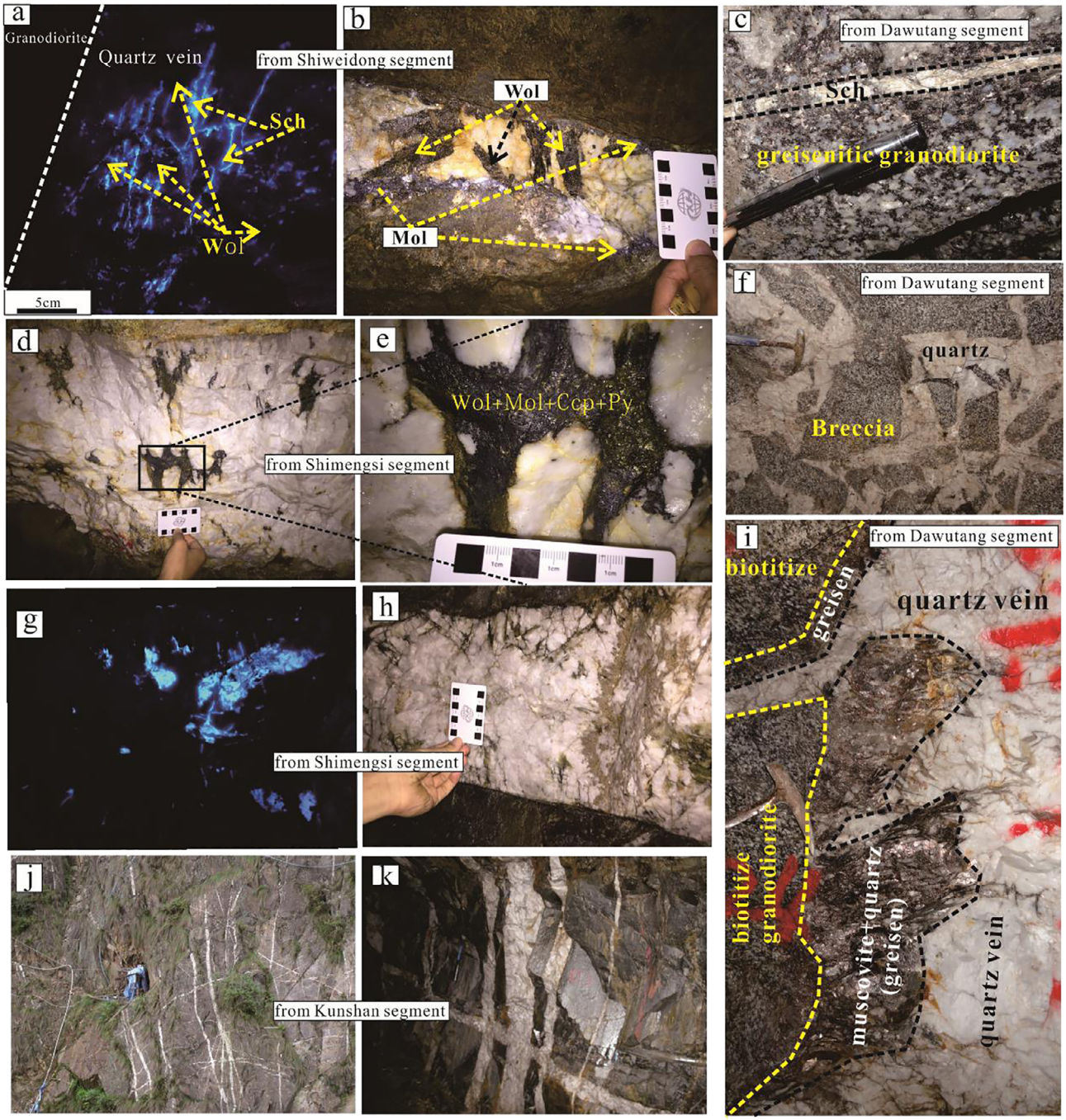

Fig. 3. Representative deposits and the alteration zoning. a, b: Quartz vein mineralization (wolframite + scheelite ± molybdenite) in the *Shiweidong* deposit. c: Scheelite vein from the *Dawutang* deposit. d, e: Quartz vein mineralization (wolframite + molybdenite + chalcopyrite ± pyrite) in the *Shimengsi* deposit. f: Hydrothermal cryptoexplosive breccia from the *Dawutang* deposit. g, h: Scheelite quartz vein mineralization in the *Shimengsi* deposit. i: Biotitization, greisen and silicic zoning in the *Dawutang* deposit. j, k: Fine quartz vein mineralization in the *Kunshan* deposit.

the greisenized granodiorite, with disseminated veinlet-type and crypto-explosive breccia in the center, both cut by quartz veins (Fig. 2b). The mineralized and biotitized granodiorite in the *Dawutang* segment is more spatially analogous to both the porphyritic granite and the hydrothermal cryptoexplosive breccia in the *Shimensi* segment. The *Dawutang* segment is a newly discovered tungsten mineralization currently being explored, with reserves of more than 0.25 Mt WO_3 (Zhang et al., 2017) and with alteration and tungsten mineralization comparable to those in the *Shimensi* segment (Fig. 2b). The *Dawutang* segment consists of porphyritic biotite granite with an exposed surface area that exceeds 200 × 400 m (Fig. 2a). The intrusive mass in the *Dawutang* segment has a core of porphyritic biotite granite, which is truncated by later fine-grained granite and then by granite porphyry.

The *Shiweidong* segment, with reserves of 0.31 Mt WO_3 (Jiang et al., 2015), consists of large quartz veins (30–100 cm width per) to disseminated veinlets (meters along the quartz vein) in the upper part, with an assemblage of quartz, wolframite, scheelite, molybdenite, chalcopyrite, and pyrite. The density of the disseminated veinlet system is less than approximately 20–30 per meter, while the veinlets range from 1 to 10 mm in width. The tungsten mineralization is mainly concentrated on the deep close to the porphyritic granite intrusive roof, with phyllic alteration ± greisenization in the granodiorite

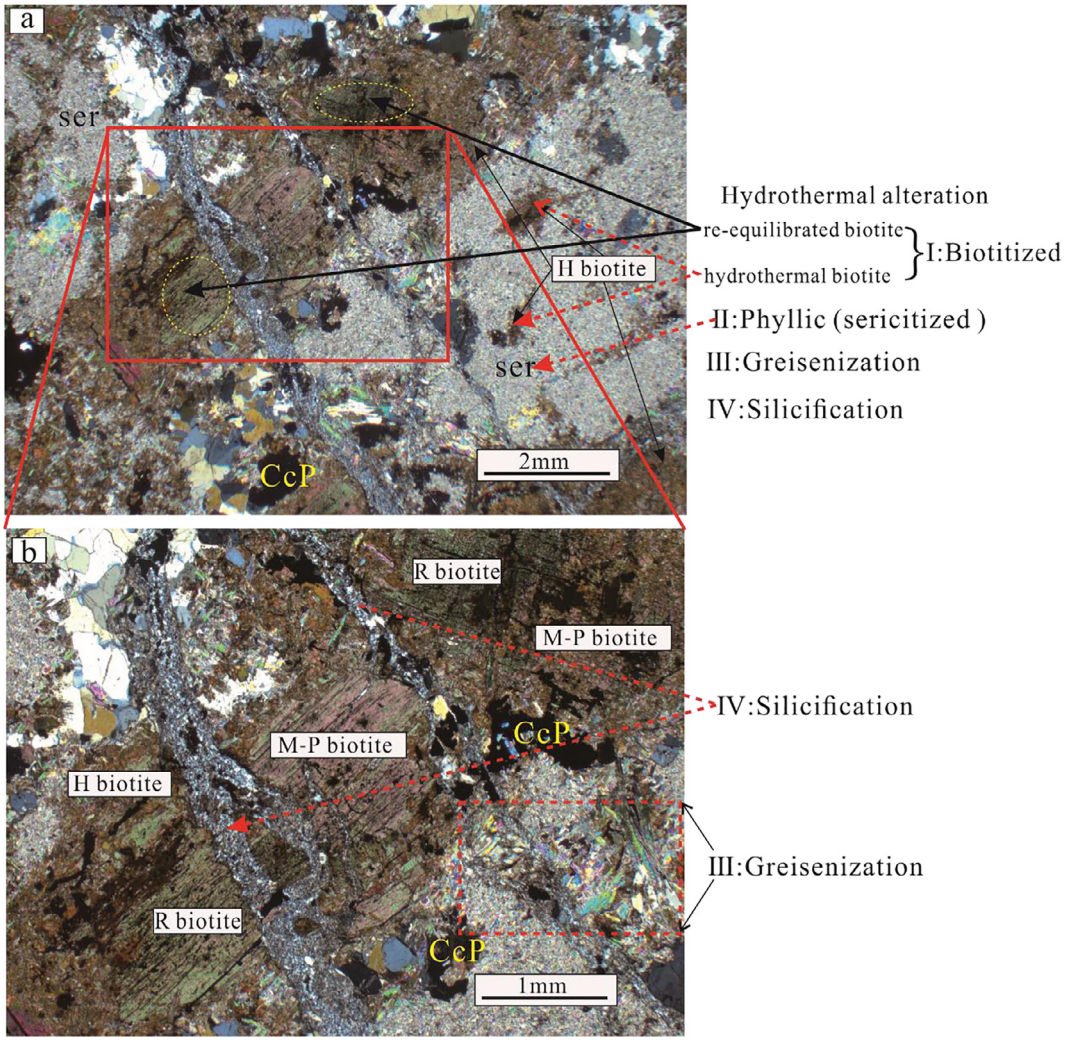

Fig. 4. Quartz veins (silicification) and examples of the four alterations found in the Dahutang tungsten deposit, including quartz (Q), fine-grained aggregate of muscovite (sericite) (ser), and chalcopyrite (Ccp) from the Jiuling biotite granodiorite. Primary biotite (P biotite), re-equilibrated biotite (R1 biotite), and hydrothermal biotite (H biotite).

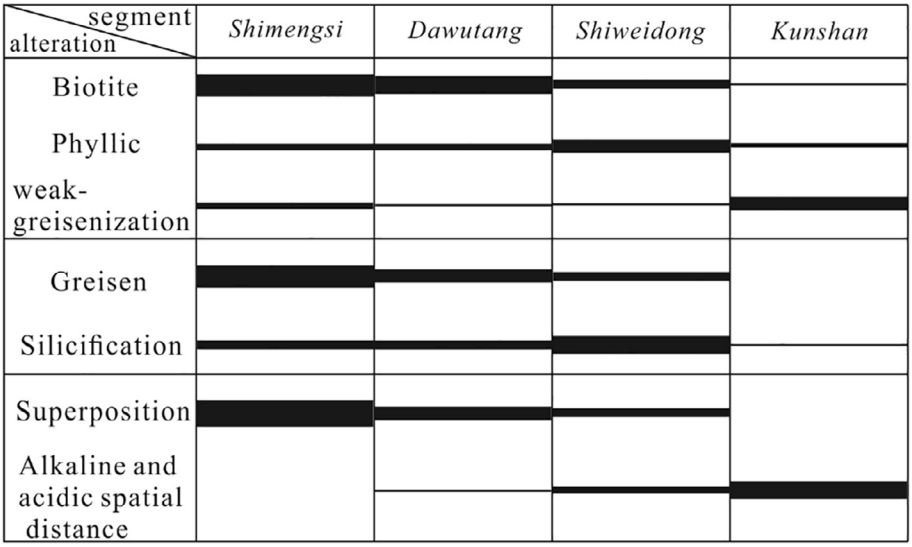

Fig. 5. Alteration zones in the four segments of the Dahutang tungsten deposit. The widths of the solid lines denote the relative abundances of alteration intensity.

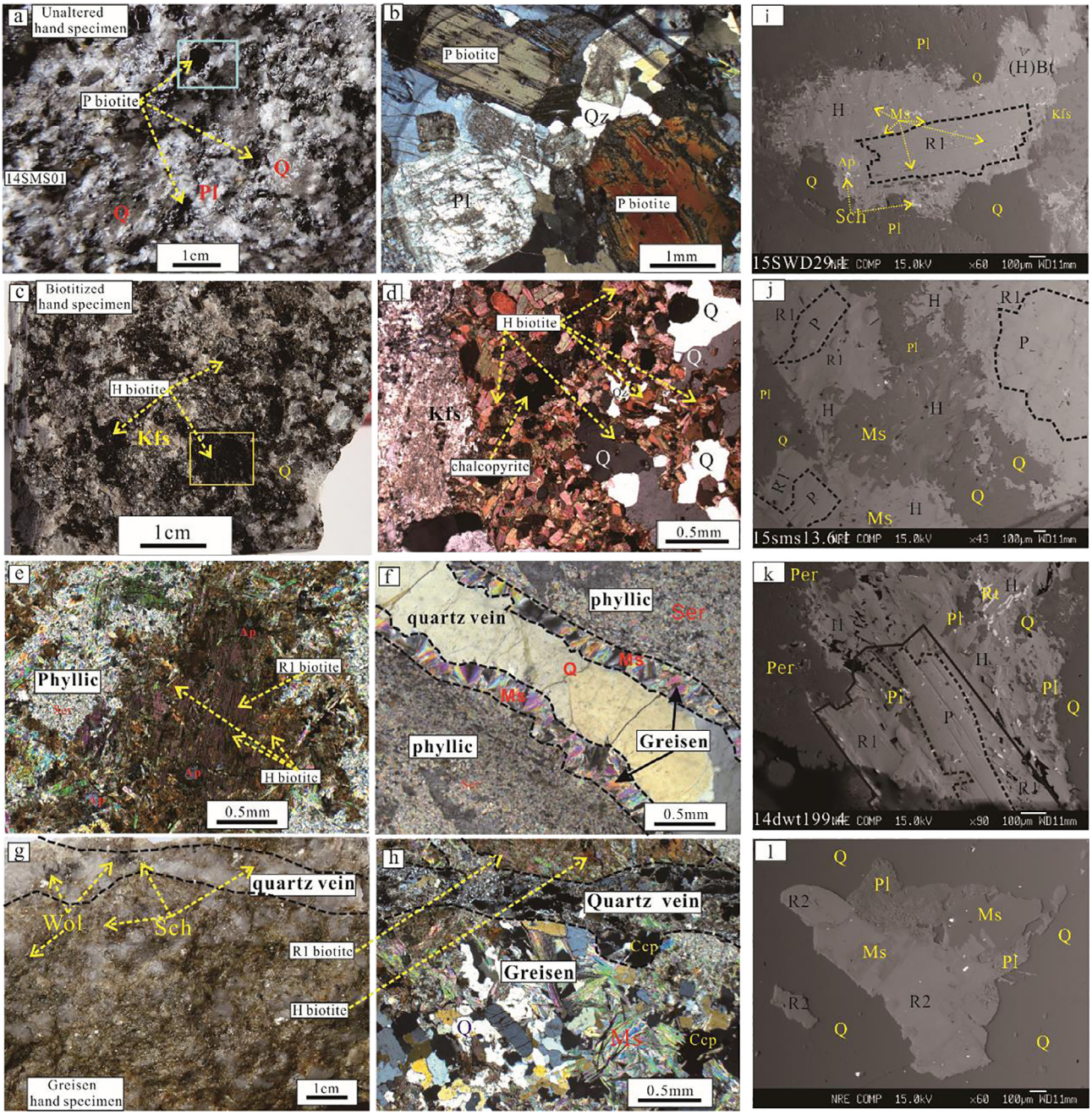

Fig. 6. Alteration types in transmitted light photomicrographs and biotite back-scattered electron images from the Dahutang deposit that show secondary biotite, (P) primary biotite from the granodiorite; (R1) re-equilibrated biotite from the granodiorite; (H) hydrothermal biotite; and (R2) re-equilibrated biotite from granite. (Q) quartz, (Kfs) K-feldspar, (ser) fine-grained aggregate of muscovite (sericite), (Ms) muscovite, (Ccp) chalcopyrite, (Mol) molybdenite, (Wol) wolframite, (Sch) scheelite, (Pl) plagioclase, (Per) Perthite, (Ap) apatite; (Rt) Rutile, (Sch) Scheelite; (Kfs) K-feldspar. a: Fresh granodiorite hand specimen. b: Euhedral primary biotite and slightly chloritized material. c: Biotitized granodiorite hand specimen. d: Secondary biotite along a quartz boundary structure. e, f: Most of the sericitization ± quartz occurs in quartz (e), biotite (e and f) and plagioclase, with the alteration zone also shown (fine-grained aggregate of muscovite (sericite), followed by the muscovite and silicification zones). g, h: Greisenization in a granodiorite hand specimen and greisen photomicrographs in transmitted light. i, j, k Biotite back-scattered electron images from the biotitized granodiorite. l: biotite back-scattered electron images from the greisenic porphyritic biotite granite.

constrained by the large quartz veins and disseminated as the veinlet-type along the large quartz veins (Fig. 2b). The *Shiweidong* segment granodiorite alteration halo that formed from the Jurassic porphyritic biotite granite as a phyllic zone, with the granodiorite intrusion, composes half of the surface area and is intruded into the other half, which is the Shuangqiaoshan Group. The Jurassic porphyritic biotite granite can be found in the adit but does not occur at the surface (Fig. 2a and b). This tungsten occurrence is present throughout the granodiorite and porphyritic biotite granite but is rare within the gray slate (see Fig. 2b).

The density of the veinlet (1–30 cm width per) system in the *Kunshan* segment ranges from 0.5 to 5 per meter (Fig. 3j and k), with the mineralization concentrated above the elevation of 500 m as a medium-scale tungsten reserve. This system is elongated in the ENE direction and is predominantly hosted by weak greisenization zones in the Jiuling granodiorite with an assemblage of quartz, muscovite, a fine-grained aggregate of muscovite (sericite), chlorite, and limonite and by the phyllic zone in the Shuangqiaoshan Group. The *Kunshan* segment consists of the altered gray slate of the Shuangqiaoshan Group

that is exposed at the surface (see Fig. 2b). In addition, some biotite alteration zones have been recognized at the bottom of the *Kunshan* segment (in drill hole ZK11-1 with an elevation of 272.5 m), approximately three hundred meters away from the ore. Both the biotite alteration and the weak greisenization formed in the Jurassic porphyritic biotite granite that intruded into the Jiuling granodiorite, but the former is deeper than the latter.

The mineralized and altered stock in the Dahutang deposit is exposed with a surface outcrop of approximately 10 km^2 and is elongated along a 7–9-km-long, NNE-trending corridor (Fig. 2a). The spatial relationship of all four segments can be directly perceived through the cross-sectional view in Fig. 2b. The outer contact zones of the porphyritic biotite granite exhibit a symmetric zonation from their center outward: biotitization + greisenization (the innermost zone of most ore bodies), biotitization ± greisenization, biotitization ± phyllic alteration, phyllic alteration, and fresh granodiorite (Fig. 2b).

After the comparative study of the alteration features in the four segments, the *Kunshan* segment contains alkaline alterations only (biotitization, phyllic alteration, and weak greisenization) (Fig. 5). In particular, the predominant alteration of weak greisenization is a slightly K_2O-enriched alkaline alteration in the *Kunshan* segment (Table 3 and Fig. 8). Only the *Kunshan* segment presents no superposition of alteration, but the other three segments have reserves corresponding to the superposition intensity (biotitization + greisenization) (Fig. 5).

4. Alteration

4.1. Biotite alteration

The biotite alteration zone is characterized by enrichment in re-equilibrated (R1) and hydrothermal (H) biotite, as a biotite ± K-feldspar ± wolframite ± apatite ± fine-grained aggregate muscovite (sericite) assemblage, and is accompanied by chlorite, ilmenite, chalcopyrite, pyrite, molybdenite, and magnetite (Fig. 6d, i, j, k). H biotite is commonly formed by the replacement of quartz phenocrysts in the granodiorite (Fig. 6c, d). The original rock texture is rarely preserved in the biotite alteration zone, and we had to go miles away to obtain some weakly altered rocks.

There are four types of biotite from the hydrothermal alteration halo of the Dahutang tungsten deposit, including primary (P) biotite, re-equilibrated (R1) and hydrothermal (H) biotite in the Jiuling (Neoproterozoic) biotite granodiorite and re-equilibrated (R2) biotite in the Jurassic porphyritic biotite granite. The P biotite in the Neoproterozoic biotite granodiorite typically occurs as euhedral to subhedral phenocrysts and/or subhedral to anhedral flakes (Fig. 5b, c, i). The R1 biotite, formed through hydrothermal metasomatism, has a shredded texture (Fig. 5b, i, j, and k). The R1 biotite is recognized by its light brown to light green colors in plane-polarized light, and some grains contain rutile needles and inclusions. The R1 biotite occurs with hydrothermal metasomatism as the re-equilibrated residue but not as the residue of primary biotite during the biotitization process. The H biotite is petrographically distinct, occurring as randomly oriented aggregates of fine-grained flakes, typically 1–10 μm in size. The H biotite, formed by the hydrothermal fluid derived from the porphyritic biotite granite, is a hydrothermal crystalline biotite. The H biotite grains are dark and small with lumpy aggregations in hand specimens (Fig. 6c). The R2 biotite of the Jurassic porphyritic biotite granite typically occurs as euhedral to subhedral phenocrysts and/or subhedral to anhedral flakes (Fig. 6l).

4.2. Phyllic alteration/weak greisenization

The phyllic alteration zone is characterized by enrichments in the fine-grained aggregates of muscovite (sericite) and quartz as a sericite ± quartz ± biotite ± muscovite ± apatite assemblage and is accompanied by wolframite, chlorite, ilmenite, and magnetite (Fig. 6e, f). A phyllic alteration zone develops along the periphery of the Jurassic porphyritic biotite granite intrusion roof in the Neoproterozoic biotite granodiorite in the *Shiweidong* segment. The phyllic alteration is overprinted by the greisen alteration (Fig. 6e, f). The *Shiweidong* segment is different from the *Shimengsi* and *Dawutang* segments, where the phyllic alteration is present along the periphery of the biotite + greisen zone and the biotite alteration zone is overprinted by phyllic zones. The phyllic zones are characterized by the replacement of most rock-forming silicates, such as plagioclase, biotite, and amphibole, by fine-grained aggregates of muscovite (sericite) + quartz. In addition, there are variable amounts of pyrite and the residues of biotitized minerals such as re-equilibrated biotite (Fig. 6e). These types of alteration change the color of the rock surface from relatively dark gray to light gray or light green. Silicification is an extensive phenomenon in this alteration zone, which adds a bleached white color to the rocks.

4.3. Greisenization

The greisenization alteration zone occurs in the Neoproterozoic biotite granodiorite spatial to the roof zone of the Jurassic porphyritic biotite granite for the fine-grained biotite granite intrusion. This zone is characterized by enrichment in muscovite, quartz, scheelite and wolframite as a muscovite + quartz ± sericite ± biotite assemblage and is accompanied by chalcopyrite, pyrite, and molybdenite (Fig. 6g, h). Greisenization overprints the biotitization core and phyllic alteration zones, which form a halo around the mineralized zones and mostly show a reduction in biotite and feldspar (Fig. 6g). These alteration minerals, which commonly form from the replacement of primary and secondary minerals via hydrothermal fluids, can permeate into any geologic body. Primary and secondary biotite phenocrysts are partially altered to muscovite and a fine-grained muscovite (sericite) aggregate (Fig. 6h). Locally, greisen is preferentially developed in the Dahutang tungsten deposit along fissures and faults. The primary rock textures in the greisenization zone are totally obscured. Our field observations show that local greisen alteration assemblages are adjacent to the ore-bearing quartz veins and the hydrothermal cryptoexplosion breccia zone (Fig. 6f, h).

4.4. Silicification

Silicification is spatially associated with the greisen alteration zone, overprinting or cutting through all the earlier alteration zones, mostly as quartz veins (Fig. 5f). This type of alteration is characterized by the occurrence of secondary quartz, chalcopyrite, molybdenite, and pyrite (Fig. 6h). These alteration minerals commonly form through the replacement of primary and secondary minerals as hydrothermal fluids penetrate the geologic body. Primary and secondary biotite phenocrysts, muscovite and a fine-grained aggregate of muscovite (sericite) are partially altered to quartz (Fig. 6f, g, h). Locally, silicification is preferentially developed in the Dahutang tungsten deposit along fissures and faults. The primary rock textures in the greisen zone are totally obscured, which indicates that local silicification assemblages are adjacent to the quartz veins at the top and around the deposit and the hydrothermal cryptoexplosion breccia zone.

4.5. Summary of the paragenetic sequence of alteration and mineralization

Based on field and microscope investigations, four stages of alteration assemblages have been identified (Fig. 7). The activity of the Jurassic porphyritic biotite granite intrusion created permeability, which allowed alkaline hydrothermal fluids to infiltrate the wall rocks, leading to diffusive biotite alteration in the Neoproterozoic Jiuling biotite granodiorite. Pervasive phyllic/weak greisenization alteration followed and partly overprinted the biotite alteration. Subsequently, acidic hydrothermal fluids infiltrated the wall rocks and formed large-

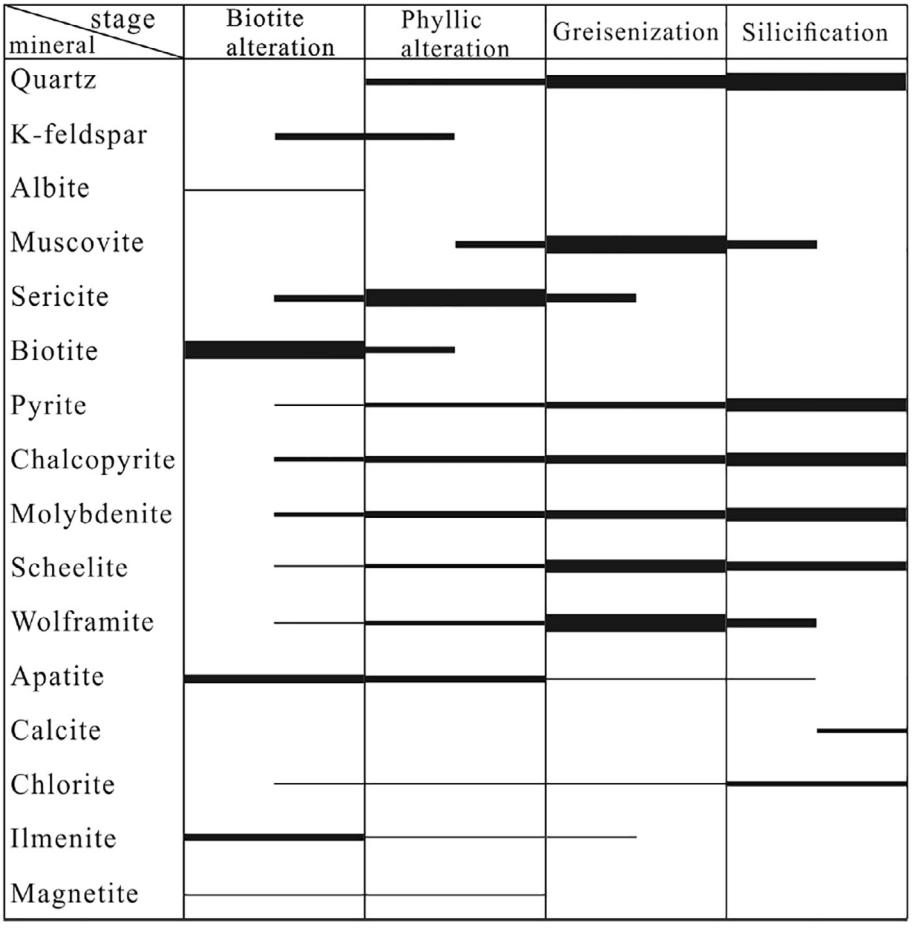

Fig. 7. Paragenetic sequence for the hydrothermal minerals of the Dahutang tungsten deposit. The widths of the solid lines denote the relative abundances of the minerals.

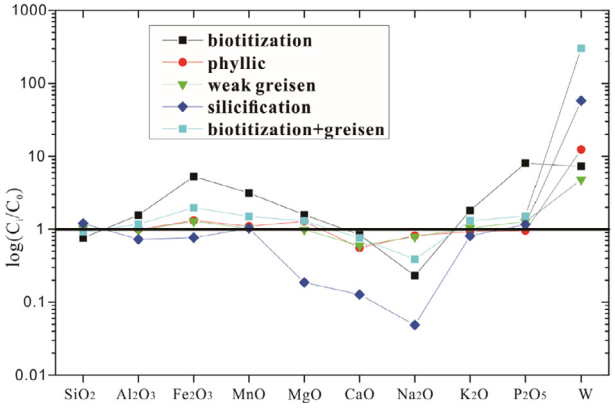

Fig. 8. Relative mass change calculations for the five types of alteration at the Dahutang deposit.

scale greisenization that mainly overprinted the biotite and phyllic alteration and later smaller-scale silicification, which mainly overprinted/cut through the former alterations. The tungsten mineralization was closely related to the greisen (muscovite + quartz) alteration. Greisenization was associated with disseminated veinlet-type ores.

5. Analytical methods

5.1. Sampling

Samples for analysis in this study were collected mainly from four boreholes (ZK68, ZK77, ZK13-5, and ZK11-1), one driftway section, and one surface geologic section. The first three boreholes are from the *Dawutang* segment, and the fourth one is from the *Kunshan* segment. The driftway section is from the *Shiweidong* segment, and the surface geologic section is from the *Shimengsi* segment. The locations, host lithologies and alteration types of the samples are provided in Supplement 1. More than 400 rocks were collected from the four segments (Fig. 2). The four alteration types can be found in the Dahutang deposit with variable superposition; the late alteration overprinted the earlier alterations, with one, two and three superposed episodes. To accurately understand the four alteration processes, we selected the end member alteration type to conduct a detailed analysis. To understand the nature of the tungsten mineralization, we selected one superposition of biotitization followed by greisenization to analyze in detail. Moreover, to accurately understand the biotitization alteration process, we selected the biotite grains, which played a key role in the alkaline alteration process, to conduct a detailed analysis.

5.2. Mineral chemistry

Biotite was identified in polished thin sections and selected from the representative alteration zones. Each thin section was examined petrographically in transmitted light and imaged in BSE mode on a scanning electron microscope (SEM) (Fig. 7). The major elements of primary magmatic and secondary alteration minerals from various rocks from drill cores, fresh rock counterparts, and adits were analyzed with a JEOL Super-probe JXA 8100 instrument at the Analytical Laboratory of the Beijing Research Institute of Uranium Geology, Beijing, China. Back-scattered electron images were obtained with the same

Table 1
Representative electron microprobe analyses of biotite from the Dahutang tungsten deposit.

Host lithology	Fresh (unaltered) granodiorite			Greisen porphyritic granite			Weakly biotitized + granodiorite			Biotitized granodiorite			
Biotite type	Primary (P)			re-equilibrated (R2)			re-equilibrated (R1)			Hydrothermal (H)			
Sample (wt%)	14SMS-01	14SMS-03	14SMS-03	15DWTZ-19	15DWTZ-39	15DWTZ-50	14ksz-50	14ksz-73	14SMS-12-2	15DWTZ-63	15DWTZ-100	14SMS-05-3	14SMS-12-2
SiO_2	35.77	34.4	33.99	35.39	35.1	35.19	35.04	35.53	34.73	35.82	35.89	35.81	34.9
TiO_2	3.95	3.82	4.9	2.18	2.18	1.98	3.12	3.08	3.12	2.51	2.07	2.17	2.29
Al_2O_3	17.55	18.25	18.38	20.85	20.71	20.9	19.1	18.86	19.15	19.91	18.91	18.53	19.43
Fe_{tot}	21	21.1	21.04	23.82	24.35	20.92	20.53	21.35	19.33	18.9	20.24	19.78	19.85
MnO	0.28	0.34	0.33	0.66	0.31	0.24	0.36	0.4	0.41	0.29	0.4	0.23	0.37
MgO	7.24	6.83	6.77	2.99	2.66	3.92	6.91	6.08	7.53	6.7	6.64	8.91	7.77
CaO	0	0.01	0	0	0	0	0	0	0	0	0	0	0.01
Na_2O	0.24	0.26	0.23	0.06	0.03	0.22	0.16	0.08	0.15	0.08	0.15	0.07	0.08
K_2O	10.17	10.27	9.96	10.32	10.1	10.26	10.51	10.56	10.33	10.07	10.33	10.39	10.21
F	0.5	0.3	0.27	1.81	0.62	3.23	0.74	0.62	0.76	1.11	2.12	0.8	0.59
Cl	0.05	0.04	0.05	0.02	0.01	0.03	0.04	0.05	0.03	–	0.03	0.03	0.03
Fe_2O_3 (cal)	4.36	4.09	4.27	5.40	4.96	5.10	2.31	2.38	4.13	4.30	4.75	4.09	4.02
FeO (cal)	17.08	17.42	17.20	18.96	19.89	16.33	18.45	19.21	15.61	15.03	15.97	16.10	16.23
H_2O (cal)	3.71	3.73	3.75	3.05	3.58	2.32	3.57	3.63	3.54	3.42	2.90	3.59	3.63
O = F, Cl	0.22	0.14	0.12	0.22	0.263	1.367	0.32	0.27	0.33	0.47	0.90	0.34	0.26
Li_2O (cal)	0.71	0.32	0.20	0.60	0.52	0.55	0.50	0.65	0.42	0.73	0.75	0.73	0.46
total	101.17	99.67	99.87	101.76	100.17	99.76	100.58	100.88	99.49	99.53	100.43	101.03	99.62
Si^{4+}	2.687	2.630	2.586	2.634	2.681	2.609	2.650	2.692	2.626	2.685	2.670	2.673	2.642
Al^{IV}	1.313	1.370	1.414	1.366	1.319	1.391	1.350	1.308	1.374	1.315	1.330	1.327	1.358
T-site	4	4	4	4	4	4	4	4	4	4	4	4	4
Al^{VI}	0.240	0.274	0.235	0.462	0.545	0.435	0.353	0.376	0.333	0.443	0.328	0.303	0.375
Ti^{4+}	0.223	0.220	0.280	0.122	0.125	0.110	0.178	0.176	0.178	0.142	0.116	0.122	0.130
Fe^{3+}	0.246	0.235	0.244	0.302	0.285	0.285	0.132	0.136	0.235	0.242	0.266	0.230	0.229
Fe^{2+}	1.073	1.114	1.095	1.180	1.271	1.012	1.167	1.217	0.987	0.942	0.994	1.005	1.027
Mn^{2+}	0.018	0.022	0.021	0.042	0.020	0.015	0.023	0.026	0.026	0.018	0.025	0.015	0.024
Mg^{2+}	0.811	0.778	0.768	0.332	0.303	0.433	0.779	0.687	0.849	0.749	0.736	0.991	0.877
Y-site	2.611	2.643	2.643	2.440	2.549	2.290	2.631	2.616	2.609	2.537	2.464	2.665	2.663
Ca^{2+}	0.000	0.001	0.000	0.000	0.000	0.000	0.000	0.000	0.000	0.000	0.000	0.000	0.001
Na^{+}	0.035	0.039	0.034	0.009	0.004	0.032	0.023	0.012	0.022	0.012	0.022	0.010	0.012
K^{+}	0.975	1.002	0.967	0.980	0.984	0.970	1.014	1.021	0.997	0.963	0.980	0.989	0.986
X-site	1.010	1.041	1.001	0.988	0.989	1.002	1.038	1.032	1.019	0.974	1.002	0.999	0.999
Cations	7.621	7.684	7.644	7.429	7.538	7.292	7.668	7.648	7.627	7.511	7.466	7.664	7.661
X_F	0.119	0.073	0.065	0.426	0.150	0.757	0.177	0.149	0.182	0.263	0.499	0.189	0.141
X_{Cl}	0.006	0.005	0.006	0.003	0.001	0.004	0.005	0.006	0.004	0.000	0.004	0.004	0.004
X_{OH}	1.011	1.008	1.008	1.030	1.000	1.053	1.015	1.013	1.014	1.018	1.036	1.015	1.012
log(XF/XOH)	−0.930	−1.143	−1.191	−0.384	−0.825	−0.143	−0.758	−0.834	−0.747	−0.588	−0.317	−0.730	−0.855
log(XCl/XOH)	−2.201	−2.289	−2.194	−2.611	−2.888	−2.446	−2.296	−2.198	−2.421	–	−2.438	−2.427	−2.420
log(XCl/XF)	0.930	1.143	1.191	0.384	0.825	0.143	0.758	0.834	0.747	0.588	0.317	0.730	0.855
$Fe^{2+}/(Fe^{2+} + Mg)$	0.570	0.589	0.588	0.781	0.807	0.700	0.600	0.639	0.538	0.557	0.574	0.503	0.540
$Mg/(Fe^{2+} + Mg)$	0.430	0.411	0.412	0.219	0.193	0.300	0.400	0.361	0.462	0.443	0.426	0.497	0.460
$100*(Fe^{2+}/Fe^{2+} + Mg)$	56.957	58.863	58.767	78.062	80.749	70.031	59.965	63.928	53.770	55.727	57.434	50.334	53.956
X_{Mg}	0.381	0.366	0.364	0.183	0.163	0.250	0.375	0.337	0.410	0.387	0.369	0.445	0.411
X_{Fe}	0.658	0.676	0.672	0.854	0.874	0.800	0.679	0.716	0.647	0.685	0.683	0.608	0.650
$\log(fH_2O/fHF)$	6.397	6.627	6.299	7.889	8.082	8.814	6.701	6.786	6.696	7.252	8.171	8.005	7.857
$\log(fH_2O/fHCl)$	5.336	5.432	5.154	6.733	6.888	7.138	5.663	5.569	5.792		6.736	6.446	6.304
$\log(fHF/fHCl)$	−1.817	−1.929	−1.822	−1.710	−1.674	−2.535	−1.855	−1.964	−1.785		−2.521	−2.732	−2.606
X_{Sid}	0.450	0.508	0.520	0.728	0.747	0.673	0.516	0.531	0.493	0.516	0.501	0.431	0.497
X_{an}	0.170	0.127	0.116	0.089	0.090	0.077	0.109	0.132	0.097	0.097	0.130	0.124	0.092
VI (F)	1.670	1.854	1.897	0.844	1.260	0.691	1.477	1.507	1.509	1.320	1.033	1.545	1.618
VI (Cl)	−3.544	−3.427	−3.520	−2.752	−2.437	−3.047	−3.437	−3.462	−3.380		−3.285	−3.442	−3.384
VI (F/Cl)	5.213	5.281	5.417	3.596	3.696	3.738	4.915	4.969	4.889		4.318	4.988	5.001

(*continued on next page*)

Table 1 (*continued*)

Host lithology	Fresh (unaltered) granodiorite			Greisen porphyritic granite			Weakly biotitized + granodiorite			Biotitized granodiorite		
Biotite type	Primary (P)			re-equilibrated (R2)			re-equilibrated (R1)			Hydrothermal (H)		
Li (cal)	0.435	0.199	0.126	0.435	0.286	0.126	0.310	0.395	0.257	0.446	0.461	0.440	0.286
OH (cal)	3.748	3.843	3.855	3.748	3.706	3.855	3.633	3.688	3.623	3.466	2.966	3.611	3.706
Fe/Fe + Mg	0.619	0.634	0.636	0.619	0.589	0.636	0.625	0.663	0.590	0.613	0.631	0.555	0.589
Geothermometry °C	605	600	650	440	440	420	551	549	560	510	450	503	500
MgO/Fe_{tot}	0.3448	0.324	0.322	0.126	0.109	0.187	0.34	0.28	0.3895	0.35	0.33	0.45	0.39
Mg-Li	0.376	0.579	0.642	−0.103	0.017	0.307	0.470	0.291	0.592	0.303	0.276	0.551	0.591
$K_2O + Na_2O$	10.41	10.53	10.19	10.38	10.130	10.48	10.67	10.64	10.48	10.15	10.48	10.46	10.29
$Fe_{tot} + Mn + Ti$	1.560	1.591	1.641	1.646	1.701	1.423	1.499	1.554	1.426	1.345	1.400	1.371	1.411
$Al^{VI} + Fe^{3+} + Ti$	0.710	0.729	0.759	0.887	24.495	0.830	0.662	0.687	0.746	0.827	0.709	0.654	0.735
$Fe^{2+} + Mn$	1.091	1.136	1.116	1.222	0.956	1.027	1.190	1.243	1.014	0.961	1.019	1.019	1.051
Log(fO_2)	−14.4	−14.8	−14.5	−17.6	−17.7	−17.8	−15.8	−15.1	−15.1	−14.0	−14.1	−13.6	−13.9
P (Mpa)	216	260	275	314	312	321	272	254	280	278	252	243	284

The crystallo-chemical formulae were calculated on the basis of 22 cation charges by using the Mica + program (Yavuz 2003). The X_{Mg} (X_{Mg} = Mg/(Mg + Fe) and X_{Fe} (X_{Fe} = (Fe + Al^{VI})/(Fe + Mg + Al^{VI})) values are mole fractions of Mg and Fe from (Zhu and Sverjensky, 1992). Methods of fluorine IV (F), chlorine IV (Cl), and fluorine/chlorine IV (F/Cl) intercept values are from (Munoz, 1984). The fugacity ratios of log (f_{H2O})/(f_{HF}), log (f_{H2O})/(f_{HCl}), and log (f_{HF})/(f_{HCl}) are calculated using the equations by (Munoz, 1992). The method of calculation for the biotite geothermometer is from (Henry, 2005), and the Log(fO_2) is from (Wones and Eugster, 1965). Ferric iron estimations as PDO are from (Dymek, 1983). The method of calculation for the biotite process is from (Uchida et al., 2007).

instrument. The analyses were conducted in WDS mode with a 15-kV accelerating voltage and 10-nA beam current. The beam diameter was approximately 1 μm. Analyses for Mg, Al, Ti, Si, Ca, Na, K, F, Cl, Mn, and Fe were conducted with Kα lines and calibrated on natural adularia, atacamite, rhodonite, titanite, fluorite, labradorite, wollastonite, and olivine. The counting times for the peaks and backgrounds (upper and lower) were 20 s and 10 s, respectively. The Li_2O content of mica was estimated based on the empirical relationships between Li_2O and SiO_2, MgO, F and Rb in trioctahedral micas (Tindle et al., 1995; Tischendorf et al., 1999; Tischendorf et al., 1997).

5.3. Whole-rock geochemistry

All the whole-rock samples and minerals were analyzed at the Analytical Laboratory of the Beijing Research Institute of Uranium Geology. The major elements were analyzed by X-ray fluorescence spectrometry (XRF) (Zhang et al., 2009). Ferric and ferrous iron measurements were determined by wet chemical analyses (titration). The analytical precision for major oxides, which were based on certified standards (GSR-1 and GSR-3) and duplicate analyses, was expressed in terms of relative percentages and ranged from ± 0.01% to ± 0.20%. The trace elements were determined by solution ICP-MS at the Analytical Laboratory of the Beijing Research Institute of Uranium Geology. Approximately 50 mg of rock powders was weighed and dissolved a mixture of distilled HF and 0.5 ml of HNO_3 (1.41 g/ml) in a Teflon-lined stainless steel bomb. The sealed bombs were then placed in an oven and heated to 190 °C for 24 h. After cooling, the bombs were opened and placed on a hotplate to evaporate to dryness at 60 °C. The residue was dissolved in a 30% HNO_3 solution, after which we resealed the bombs and heated them at 130 °C for 3 h. The final solutions were migrated into plastic beakers and diluted before analysis. The detailed sample preparations, instrument operating conditions and calibration procedures followed Liang and Grégoire (2000) and Gao (2003). Two standards (granite GSR-1 and basalt GSR-3) were used to monitor the analytical quality of the data.

6. Results

6.1. Mineral chemistry

The biotite that was identified in the polished thin sections was analyzed (Table 1) to determine the chemical compositions of each biotite type and to understand the conditions under which the biotite formed. We used the Micaplus computer program (Yavuz, 2003) to classify the biotites from the Dahutang deposit as dioctahedral micas according to their chemical affinities. A variety of parameters were calculated for mica with this program (Table 1). Micaplus converts oxides to elements based on 22 cations, which are allocated into the I, M, T, and A sites. The H biotite is characterized by the highest amounts of X_{Mg}, Al_2O_3 and K_2O. The R1 biotite is characterized by the highest amounts of FeO but the lowest amounts of Fe_2O_3. The lowest amount of Al_2O_3 and highest content of TiO_2 are found in the P biotite (unaltered Jiuling biotite granodiorite) (Table 1). All the X_{Mg} values vary between 0.18 and 0.41, increasing from R2 to R1, P and H. The K_2O contents tend to increase from primary (P) to re-equilibrated (R1) and then decrease to hydrothermal (H) biotite (Table 1). The primary biotite of the granodiorite shows a high level of TiO_2 (3.82–4.9 wt%) compared to the R1 (3.08–3.12 wt%), H (2.07–2.51 wt%), and R1 (1.98–2.18 wt%) biotite (Table 1).

6.2. Whole-rock geochemistry

6.2.1. Fresh (unaltered) granodiorite

The SiO_2 content of fresh (unaltered) granodiorite samples ranges from 65.85 to 68.11 wt%; MgO, from 0.65 to 1.85 wt%; Fe_2O_3, from 0.42 to 0.99 wt%; MnO, from 0.06 to 0.12 wt%; Na_2O, from 2.28 to

Table 2
Analytical results for the granodiorite from the Dahutang tungsten deposit (for detailed data, see the Supplement 1).

Alteration type/ Host lithology	Unaltered (8)			Biotitization (7)			Phyllic (9)			Weak Greisenization (7)			Silicification (1)	Biotitization + strong Greisenization (8)		
	min	max	average	min	max	average	min	max	average	min	max	average		min	max	average
SiO_2	65.85	68.11	67.00	44.92	60.23	51.00	66.45	68.72	67.79	66.22	71.93	69.07	80.56	48.45	68.18	61.75
TiO_2	0.292	0.649	0.49	0.027	0.895	0.53	0.525	0.594	0.56	0.316	0.777	0.50	0.47	0.473	0.684	0.59
Al_2O_3	13.89	15.83	15.20	17.36	30.5	23.76	14.55	15.64	15.09	13.77	15.65	14.74	11.06	14.21	25.6	17.77
Fe_2O_3	0.42	0.99	0.70	0.94	7.81	3.18	0.53	1.03	0.79	0.22	1.16	0.77	0.46	0.78	1.65	1.19
MnO	0.062	0.115	0.09	0.096	0.467	0.25	0.066	0.112	0.09	0.046	0.116	0.08	0.08	0.083	0.197	0.12
MgO	0.652	1.85	1.26	0.885	3.83	1.99	1.37	1.92	1.62	0.607	1.98	1.24	0.24	1.15	1.90	1.64
CaO	1.23	4.74	2.24	0.535	3.00	1.89	0.747	1.69	1.25	0.718	1.90	1.34	0.29	1.1	2.14	1.70
Na_2O	2.28	2.98	2.54	0.197	1.80	0.59	1.05	2.66	2.08	0.419	3.41	2.00	0.12	0.272	2.59	0.99
K_2O	3.21	4.93	4.16	5.94	9.82	7.49	3.49	4.18	3.86	3.67	4.84	4.32	3.36	3.68	8.26	5.43
P_2O_5	0.115	0.176	0.14	0.072	2.26	1.12	0.122	0.148	0.13	0.108	0.344	0.18	0.16	0.15	0.438	0.21
Ni	4.11	28.4	17.12	3.57	37.5	18.75	20.4	24.8	23.03	4.08	32.5	16.32	1.90	22.0	30.6	25.93
V	28.9	98.9	64.80	1.47	106	67.14	63.6	76.3	68.93	28.5	98.6	60.51	6.08	64.7	97	79.79
Sc	4.86	14.9	9.82	1.83	17.7	11.85	7.93	12.2	10.77	5.33	17.0	10.45	2.40	10.3	16.5	13.13
Lu	0.183	0.428	0.28	0.026	0.544	0.35	0.249	0.474	0.32	0.213	0.47	0.29	0.16	0.248	0.661	0.36
Co	4.47	14.4	10.71	5.42	21.1	13.51	10.4	14.5	11.93	4.36	15.5	8.81	2.56	10.4	16.2	13.50
W	1.83	13	9.65	37.9	172	70.03	11.7	268	119.62	7.01	138	46.24	558.00	228	7342	2922.75

Table 3
Summary of major and trace elements in granodiorite samples from the Dahutang tungsten deposit.

Alteration type	Biotitization			Phyllic			Weak Greisenization			Silicification			Biotitization + strong Greisenization		
Mass change	ΔC_i	$\Delta C_i/C_0$	C_i/C_0	ΔC_i	$\Delta C_i/C_0$	C_i/C_0	ΔC_i	$\Delta C_i/C_0$	C_i/C_0	ΔC_i	$\Delta C_i/C_0$	C_i/C_0	ΔC_i	$\Delta C_i/C_0$	C_i/C_0
SiO_2	−15.72	−0.23	0.76	0.05	0.00	1.01	2.14	0.03	1.03	17.45	0.26	1.20	−4.24	−0.06	0.92
Al_2O_3	8.69	0.57	1.56	−0.27	−0.02	0.99	−0.45	−0.03	0.97	−3.61	−0.24	0.73	2.86	0.19	1.17
Fe_2O_3	2.60	4.33	5.30	0.18	0.30	1.32	0.17	0.28	1.28	−0.12	−0.20	0.77	0.60	1.01	1.98
MnO	0.17	2.16	3.15	0.01	0.09	1.10	0.00	0.03	1.03	0.01	0.08	1.03	0.04	0.53	1.50
MgO	0.74	0.59	1.58	0.34	0.27	1.28	−0.02	−0.02	0.98	−1.02	−0.80	0.19	0.40	0.32	1.30
CaO	−0.34	−0.15	0.84	−1.00	−0.45	0.56	−0.90	−0.40	0.60	−1.94	−0.87	0.13	−0.51	−0.23	0.76
Na_2O	−1.95	−0.77	0.23	−0.49	−0.19	0.82	−0.54	−0.21	0.79	−2.41	−0.95	0.05	−1.54	−0.60	0.39
K_2O	3.38	0.81	1.80	−0.34	−0.08	0.93	0.17	0.04	1.04	−0.63	−0.15	0.81	1.36	0.33	1.31
P_2O_5	0.99	7.07	8.03	−0.01	−0.05	0.96	0.04	0.27	1.27	0.03	0.22	1.16	0.08	0.54	1.52
W	60.76	6.30	7.26	108.66	11.26	12.40	36.64	3.80	4.79	575.33	59.63	57.83	2961.36	306.91	302.91

ΔC_i calculated by the Excel program from López-Moro (2012); ΔCi (absolute gain/loss in wt% or ppm) and ($\mathbf{\Delta C_i/C_0}$ and $\mathbf{C_i/C_0}$) (relative mass change).

2.98 wt%; and K_2O, from 3.43 to 4.93 wt%. The fresh granodiorite is also characterized by low contents of Al_2O_3 (13.89–15.83 wt%, mean: 15.20 wt%), P_2O_5 (0.11–0.17 wt%, mean: 0.14 wt%), and low concentrations of W (1.83–13.0 ppm, mean: 9.65 ppm) (Tables 2 and Supplement 1).

6.2.2. Altered granodiorite

The SiO_2 content of the **biotitized** granodiorite samples from the *Dawutang* and *Kunshan* segments ranges from 44.92 to 60.23 wt% (mean: 51.00 wt%), with large amounts of SiO_2 and Na_2O (0.20–1.8 wt %, mean: 0.59 wt%) decreasing. They have relatively low content of CaO (0.54– 3.00 wt%, mean: 1.89 wt%), while they are enriched in MgO (0.89–3.83 wt%, mean: 1.99 wt%), Fe_2O_3 (0.94–7.81 wt%, mean: 3.18 wt%), MnO (0.10–0.47 wt%, mean: 0.25 wt%), and K_2O (5.94–9.82 wt%, mean: 7.49 wt%) (Tables 2 and Supplement 1). The Al_2O_3 (17.36–30.5 wt%, mean: 23.76 wt%) and P_2O_5 (0.07–2.26 wt%, mean: 1.12 wt%) in the biotitized granodiorite samples gradually increased. Those biotitized granodiorite samples are enriched in W (37.9–172 ppm, mean: 70.3 ppm), approximately ten times the values of the fresh samples.

The SiO_2 contents of **phyllic** granodiorite samples from the *Shiweidong* and *Dawutang* segments range from 66.45 to 68.72 wt% (mean: 67.79 wt%) with little increase in SiO_2 compared with the fresh rock; these samples are slightly enriched in MgO (1.37–1.92 wt%, mean: 1.62 wt%), Fe_2O_3 (0.53–1.03 wt%, mean: 0.79 wt%), MnO (0.07–0.11 wt%, mean: 0.09 wt%), and K_2O (3.49–4.18 wt%, mean: 3.86 wt%) (Tables 3 and Supplement 1). The Al_2O_3 (14.55–15.64 wt%, mean: 14.74 wt%) and P_2O_5 (0.12–0.15 wt%, mean: 0.13 wt%) in the phyllic granodiorite samples gradually increases compared to those for the fresh rock; the SiO_2 increases, but CaO, Na_2O, and K_2O decrease (see Table 2). These phyllic granodiorite samples are enriched in W (11.7–268 ppm, mean: 119.62 ppm) to a higher degree than the biotitized granodiorite samples.

The SiO_2 contents of the **weakly greisenized** granodiorite samples from the *Kunshan* and *Shimengsi* segments, far from the contact zone deposit, range from 66.22 to 71.93 wt%, with a mean of 69.07 wt%; these samples show an obvious increase in SiO_2 but decreases in MgO (0.61–1.98 wt%, mean: 1.24 wt%), Al_2O_3 (13.77–15.65 wt%, mean: 14.74 wt%), Fe_2O_3 (0.22–1.16 wt%, mean: 0.77 wt%), and MnO (0.05–0.12 wt%, mean: 0.08 wt%), compared with the fresh rock. These samples are also slightly enriched in K_2O (3.67–4.84 wt%, mean: 4.32 wt%) and P_2O_5 (0.11–0.34 wt%, mean: 0.18 wt%) (Tables 3 and Supplement 1). These greisenized granodiorite samples are enriched in W (7.01–138 ppm, mean: 46.24 ppm) and have concentrations that are tens to hundreds of times those of the fresh samples.

The **silicified** granodiorite samples from the *Dawutang* segment are enriched in SiO_2 (80.56 wt%) and CaO (0.29 wt%) compared to the fresh (unaltered) rock, and the contents of Al_2O_3, Fe_2O_3, MnO, MgO, Na_2O, K_2O, and P_2O_5 are reduced (Tables 3 and Supplement 1). The silicified granodiorite samples are enriched in W (558 ppm, hundreds of

times the values of the fresh samples).

The SiO_2 contents of the **biotitized + greisenized** granodiorite samples from the *Shimengsi* and *Dawutang* segments range from 48.45 to 68.18 wt% (mean: 61.75 wt%), lower than those of the fresh rock but higher than those of the biotitized rock. The Al_2O_3 (14.21–25.60 wt%, mean: 17.77 wt%) and P_2O_5 (0.15–0.44 wt%, mean: 0.21 wt%) values are higher than those of the fresh rock but lower than those of the biotitized rock. The biotitized + greisenized granodiorite samples are slightly enriched in MgO (1.15–1.90 wt%, mean: 1.64 wt%), Fe_2O_3 (0.78–1.65 wt%, mean: 1.19 wt%), MnO (0.08–0.20 wt%, mean: 0.12 wt%), and K_2O (3.68–8.26 wt%, mean: 5.43 wt%) compared to the fresh rock (Tables 2 and Supplement 1). It is obvious that in the biotitized + greisenized granodiorite samples, the SiO_2 contents gradually increase compared to those of the biotitized rock. These biotitized + greisenized granodiorite samples are enriched in W (228–7342 ppm, mean: 2922.75 ppm, hundreds to thousands times the values of the fresh samples) and are also hundreds of times enriched in W compared to the biotitized sample.

7. Discussion

7.1. Element changes during the alteration process

Mass balance calculations have provided an important and useful method to understand geological process, especially the absolute mass gain/loss of elements in hydrothermal systems. The idea of modeling mobility/immobility in a system was first reported by Gresens (1967), and the immobile element approaches have been developed by Maclean (1987, 1988, 1990). Because choosing an accurate immobile element is difficult, we use the binary correlation plots by Klammer (1997) to determine the immobile elements during the hydrothermal alteration at the Dahutang tungsten deposit (for choosing the immobile elements, see the Supplement 1). In this paper, we choose TiO_2, Ni, V, Sc, Lu, and Co as the most immobile elements.

The main advantages of the graphical methods are their rapid implementation and the clarity of the diagrams (Durand et al., 2015). The isocon method of Grant (1986) was used to demonstrate potential chemical changes between altered wall rocks and their corresponding "protoliths/unaltered rocks". Therefore, we choose the graphical methods and the deuterogenic program "EASYGRESGRANT", a user-friendly interactive Microsoft Excel spreadsheet program by López-Moro (2012). All the calculations follow Grant's approach (Grant, 1986):

$$\Delta C = (C_i^F / C_i^A) \cdot C^A - C^F$$

where C^F and C^A are the concentrations in the fresh (F) and altered (A) sample, respectively, and ΔC denotes the gain or loss in grams per 100 g of rock for major elements or in parts per million for trace elements, "*i*" is the immobile element. The results are presented in Table 3.

7.1.1. Biotitization

The biotitized granodiorite from the *Dawutang* and *Kunshan* segments exhibit strong depletion in SiO_2 ($\Delta C_i = -15.72$ wt%) and weak loss of Na_2O ($\Delta C_i = -1.95$ wt%) and CaO ($\Delta C_i = -0.34$ wt%) but enrichment in MgO ($\Delta C_i = 0.74$ wt%), Fe_2O_3 ($\Delta C_i = 2.60$ wt%), MnO ($\Delta C_i = 0.17$ wt%), P_2O_5 ($\Delta C_i = 0.99$ wt%), and K_2O ($\Delta C_i = 3.38$ wt%) (Table 2). During biotitization, W shows significant enrichment ($\Delta C_i = 60.76$ ppm).

The elements Fe, Mn, P, Na, and W exhibit strong mobility ($\Delta C_i/C0 > 1.0$ or $-0.5 > \Delta C_i/C_0$) into the biotitized rock during the biotitization process (Table 3 and Fig. 8), which is confirmed by the formation of hydrothermal biotite and apatite (Fig. 6i). The elements Al, K and Mg exhibit moderate mobility ($1.0 > \Delta C_i/C_0 > 0.1$) into the altered rock. Sodium is apt to move out of the altered rock during the biotitization process (Table 3). The mobility of Si and Ca out of the altered rock is moderate ($-0.1 > \Delta C_i/C_0 > -0.5$) during the biotitization process (Table 3).

The elements Al, Fe, Mn, Mg, K, and P migrated into the biotitized rock, and large amounts of Si and Na migrated out, which indicates an oxidized high-temperature alkaline solution. The elements Fe, Mn and P moved into the altered rock to form large amounts of hydrothermal (H) biotite and apatite, which functioned as storage places; later, these elements were released by acidic alteration (all four types of biotite changed to muscovite) and formed wolframite and scheelite in the greisenic rock (Table 1).

The elements Al, Fe^{3+}, Mn, Mg, K, P, and W migrated in, and Si, Ca, and Na migrated out of the rock during the biotitization alteration process. The elements Ti, Ni, V, Sc, and Lu exhibited weak mobility (immobile) for all five alteration processes (see Supplement 1). The Na that moved into the fluid could cause a change from K_2WO_4 to Na_2WO_4. The solubility of Na_2WO_4 is half that of K_2WO_4 (Liu and Ma, 1987). This difference in solubility may lead to the enrichment of the element W in biotitized rock (Fig. 9b).

7.1.2. Phyllic

The phyllic granodiorite samples exhibit moderate depletion in CaO ($\Delta C_i = -1.00$ wt%), K_2O ($\Delta C_i = -0.34$ wt%), Al_2O_3 ($\Delta C_i = -0.27$ wt%), P_2O_5 ($\Delta C_i = -0.01$ wt%), and Na_2O ($\Delta C_i = -0.49$ wt%), from the *Shiweidong* and *Shimengsi* segments. There were slight increases in SiO_2 ($\Delta Ci = 0.05$ wt%), MgO ($\Delta C_i = 0.34$ wt%), Fe_2O_3 ($\Delta C_i = 0.18$ wt%), and MnO ($\Delta C_i = 0.01$ wt%) (Tables 3 and Supplement 1). These phyllic granodiorite samples show significant enrichment in W ($\Delta C_i = 108.66$ ppm).

The element W exhibited strong mobility during the phyllic alteration process (Table 3 and Fig. 8). In contrast, Ca moved into fluid from the phyllic rock.

The elements Fe, Mg and W migrated in, and Ca, Mn, K, Na, and P migrated out during the phyllic process, which indicates lower oxidization than for the biotitization process (Fig. 9b and d). The elements Si, Al, Ti, Ni, V, Sc, and Lu exhibited weak mobility (immobile) during the phyllic alteration process (see Table 3, Fig. 9d, and Supplement 1).

7.1.3. Weak greisenization

The Weak greisenization can be defined by the gain of SiO_2 ($0 < \Delta Ci < 5.0$ wt%), and original mineral partly altered to muscovite and quartz weakly along the edge of the mineral. The weakly greisenized granodiorite samples from the *Kunshan* and *Shimengsi* segments exhibited moderate enrichments in SiO_2 ($\Delta C_i = 2.14$ wt% < 5.0 wt%, and original mineral partly altered to muscovite and quartz), Fe_2O_3 ($\Delta C_i = 0.17$ wt%), K_2O ($\Delta C_i = 0.17$ wt%), P_2O_5 ($\Delta C_i = 0.04$ wt%), and W ($\Delta C_i = 36.64$ ppm) and depletions in MgO ($\Delta C_i = -0.02$ wt%), Na_2O ($\Delta C_i = -0.54$ wt%) and CaO ($\Delta C_i = -0.90$ wt%) (Tables 2 and Supplement 1). The elements Al, Mn, Ti, Ni, V, Sc, and Lu exhibited weak mobility (immobile) at the weak greisenization stage (see Tables 3 and Supplement 1).

The elements Al and Si exhibited weak mobility but showed different behaviors. Aluminum moved out, while silica moved into the altered rock during the weak greisenization alteration process (Table 3 and Fig. 8). Mg and K exhibited weak mobility but also showed different behaviors. Magnesium moved out, while potassium moved into the altered rock. The moderate mobility elements Ca and Na mobilized out of the altered rock, while Fe and P mobilized into the altered rock; changes in both elements were lower than those during the biotite alteration; only the element W exhibited strong mobility, which indicates a deoxidizing alkaline fluid that might have played an important role in wolframite deposition (c.f. (Liu and Ma, 1987)), (Fig. 9c and e).

7.1.4. Silicification

The silicified granodiorite samples were depleted in most of the major elements but enriched in SiO_2 ($\Delta C_i = 17.45$ wt%) and W ($\Delta C_i = 578.59$ ppm) in the *Dawutang* segment (Table 3). The elements

Mg, Ca, Na and W exhibited moderate mobility; Mg, Ca, Na moved out, while W moved into the altered rock during silicification (Table 3, Fig. 8, and Fig. 9f). The moderate mobility elements Si and P mobilized into the altered rock, while Al, Fe, and K mobilized out of the altered rock, indicating a deoxidizing moderate- to low-temperature acidic solution (Fig. 9f).

7.1.5. Biotitization + greisenization

The biotite + greisen altered granodiorite samples from the *Dawutang* and *Shimengsi* segments exhibited depletion in SiO_2 ($\Delta C_i = -4.24$ wt%), CaO ($\Delta C_i = -0.51$ wt%) and Na_2O ($\Delta C_i = -1.54$ wt%), and enrichment in MgO ($\Delta C_i = 0.40$ wt%), Fe_2O_3 ($\Delta C_i = 0.60$ wt%), MnO ($\Delta C_i = 0.04$ wt%), P_2O_5 ($\Delta C_i = 0.08$ wt%), and K_2O ($\Delta C_i = 1.36$ wt%) (Tables 2 and Supplement 1). It is noted that biotitized + greisenized granodiorite samples are characterized by extreme enrichment in W ($\Delta C_i = 2961.36$ ppm), indicating that the superposition of biotitization by greisenization might be critical for the tungsten mineralization at Dahutang (Fig. 9b and c).

7.2. Alkaline alteration recorded by biotite

7.2.1. Biotite chemical composition of fluids/agents

The alkaline altered Jiuling biotite granodiorite contains a mass of biotite with recrystallization (R1) or hydrothermal (H) origins. The acidic alteration formed secondary biotite as well. The biotite crystals has variable compositions and thus recorded the chemical composition and physical conditions of the acidic fluids.

All the studied biotites clustered in the Fe biotite field have a distinct eastonite composition (Fig. 10), unlike the Mg biotites in igneous rocks that are generally associated with porphyry copper deposits (Afshooni et al., 2013; Einali et al., 2014; Moore and Czamanske, 1973; Parsapoor et al., 2015; Selby and Nesbitt, 2000). Fe biotite can act as a storage place for Fe-Mn and also indicates a fluid rich in Fe, which is good for wolframite to be deposited from the fluid (Liu and Ma, 1987). All the studied biotites are characterized by relatively low Cl content (0–0.05) compared to those of the typical porphyry copper deposits (Afshooni et al., 2013; Parsapoor et al., 2015), which is very consistent with the obtained results for similar chemical features of biotite from Sn-W-Be systems. That the biotites show an F-rich system rather than a Cl-rich system does not agree with the deposition of scheelite and the dissolution of quartz to the fluid, as a desilification process (Liu and Ma, 1987). There are high values of F in log(fHF/fHCl) and log(fH_2O/fHCl) in the Dahutang tungsten deposit (Table 1). High values of F in log(fHF/fHCl) can suppress the deposition of scheelite, but high values of log(fH_2O/fHCl) can promote the extreme hydrolyzation of plagioclase to release Ca to the fluid, which is positive for the deposition of scheelite from the fluid (Liu and Ma, 1987).

7.2.2. The oxygen fugacity during the alkaline alteration process

Wones and Eugster (1965) proposed that the magnesium-rich trend in the biotite compositions represents increasing f_{O2} (through the loss of hydrogen) and leads to an increase in the amount of magnetite present and in the Mg-Fe ratios of the associated ferromagnesian phases. Therefore, the oxygen fugacity values (fO_2) can relatively correspond to the Mg/Fe ratios and the Fe_2O_3 (cal) content of the biotite. The biotite of the Dahutang deposit falls above the Fe_2O_3–F_3O_4 (HM) oxide buffer in the Fe^{3+}–Fe^{2+}–Mg diagram of Wones and Eugster (1965). The hydrothermal biotite in the alkaline (biotitized) altered rocks has Mg/(Fe^{2+} + Mg) ratios higher than those in both the primary and re-equilibrated biotite in the granodiorite, indicating a higher oxygen fugacity during alkaline alteration. This factor corresponds to the increase in Fe^{3+} in the alkaline altered rock.

Different types of biotite have a decreasing trend for oxygen fugacity (H → P→R1 → R2), indicative of decreasing oxygen fugacity in the fluid system. This interpretation is consistent with the oxygen fugacity variations recorded in apatite in the granite in the Dahutang tungsten deposit (Han et al., 2016). High oxygen fugacity during the biotitization process is not favorable for wolframite deposition. As the oxygen fugacity decreased during the greisenization process, wolframite could form from the hydrothermal fluids.

7.2.3. Temperature of the alkaline alteration process

The solubility of Ti in primary biotite is generally controlled by temperature and pressure so that the Ti content in biotite can be used to deduce the temperature and pressure when the biotite crystallized.

The concentration of Ti in biotite is very sensitive to temperature, so we can use biotite to obtain reliable temperature estimates in igneous and metamorphic rocks (Douce, 1993). There are decreasing TiO_2 contents from primary biotite (ranging from 3.82 to 4.9 wt%) to re-equilibrated biotite (R1) (ranging from 3.08 to 3.12 wt%). In addition, both hydrothermal (H) biotite and porphyritic granite altered biotite (R2) have lower TiO_2 contents than re-equilibrated biotite, indicating relatively high temperature. We used the empirical Ti-in-biotite geothermometer of Henry (2005) to calculate the plutonic and hydrothermal biotite precipitation temperatures (Eq. (1)). The compositions of biotites from the Dahutang samples fall within the calibrated compositional, temperature, and pressure ranges that are specified for the geothermometer (X_{Mg} = 0.275–1.000, Ti = 0.04–0.60 apfu, T = 480–800 °C, and 400–600 MPa) (Table 1).

$$T = ([\ln(Ti) - a - c(X_{Mg})/b])^{0.33} \quad (1)$$

Coefficient values: a = 2.3594; b = 4.6482e − 9; c = −1.7283.

The calculated temperatures for the different types of biotite ranged from 600 to 650 °C (P), 550 to 560 °C (R1), 450 to 510 °C (H), and 420 to 440 °C (R2) for the greisen alteration (an acidic hydrothermal type) (Table 1). These data indicate that the primary biotite is characterized by higher temperatures (greater than 600 °C) for the diagenesis of the Jiuling biotite granodiorite. However, the R1 biotite crystallized at temperatures from 500 to 560 °C for hydrothermal alteration, and the H biotite crystallized at lower temperatures (450–510 °C); both of these biotites formed by the alkaline hydrothermal alteration of biotite.

Mineralogical and fluid inclusion (mostly in quartz) analyses suggested that the temperatures of the silicification hydrothermal alteration ranged from 372 to 160 °C (Jiang, 2016; Ruan et al., 2015; Xu, 2013; Zhang, 2013). Consequently, we suggest three distinct hydrothermal fluids as follows: The first hydrothermal fluid caused alkaline (biotitization) alteration and Fe + Mn ± W mineralization at temperatures ranging from 560 to 450 °C. This fluid was a magmatic hydrothermal fluid derived from the Cretaceous porphyritic granite and characterized by high pH, moderate pressure (Table 1), and low salinity. The second hydrothermal fluid was formed by the mixing of magmatic fluid with meteoric water. This fluid was responsible for the phyllic and weak greisenization alteration zones and the Cu + Mo mineralization at temperatures ranging from 440 to 450 °C. The third hydrothermal fluid caused acidic (greisenization and silicification) alteration and W + Cu + Mo mineralization at temperatures ranging from 440 to 160 °C. This fluid was characterized by high pressure and moderate to low salinity. The fluid was derived from the Cretaceous fine-grained biotite granite and associated with the main W mineralization at Dahutang.

7.3. The effect of superposition of alkaline by acidic hydrothermal alteration in tungsten mineralization

Elements can be transported in/out during hydrothermal alteration, which is responsible for alteration and mineralization processes. For example, the replacement of biotite by muscovite in the granite can release large amounts of Fe, Mn, Sn and W (Azadbakht et al., 2014; Barsukov, 1957; Chen et al., 2010; Eugster, 1985; Lentz, 1992; Li et al., 2015; Neves, 1997; Pirajno, 1982; Shcherba, 1970; Taylor, 1979; Yang and Rivers, 2000). The hydrolyzation of plagioclase can release

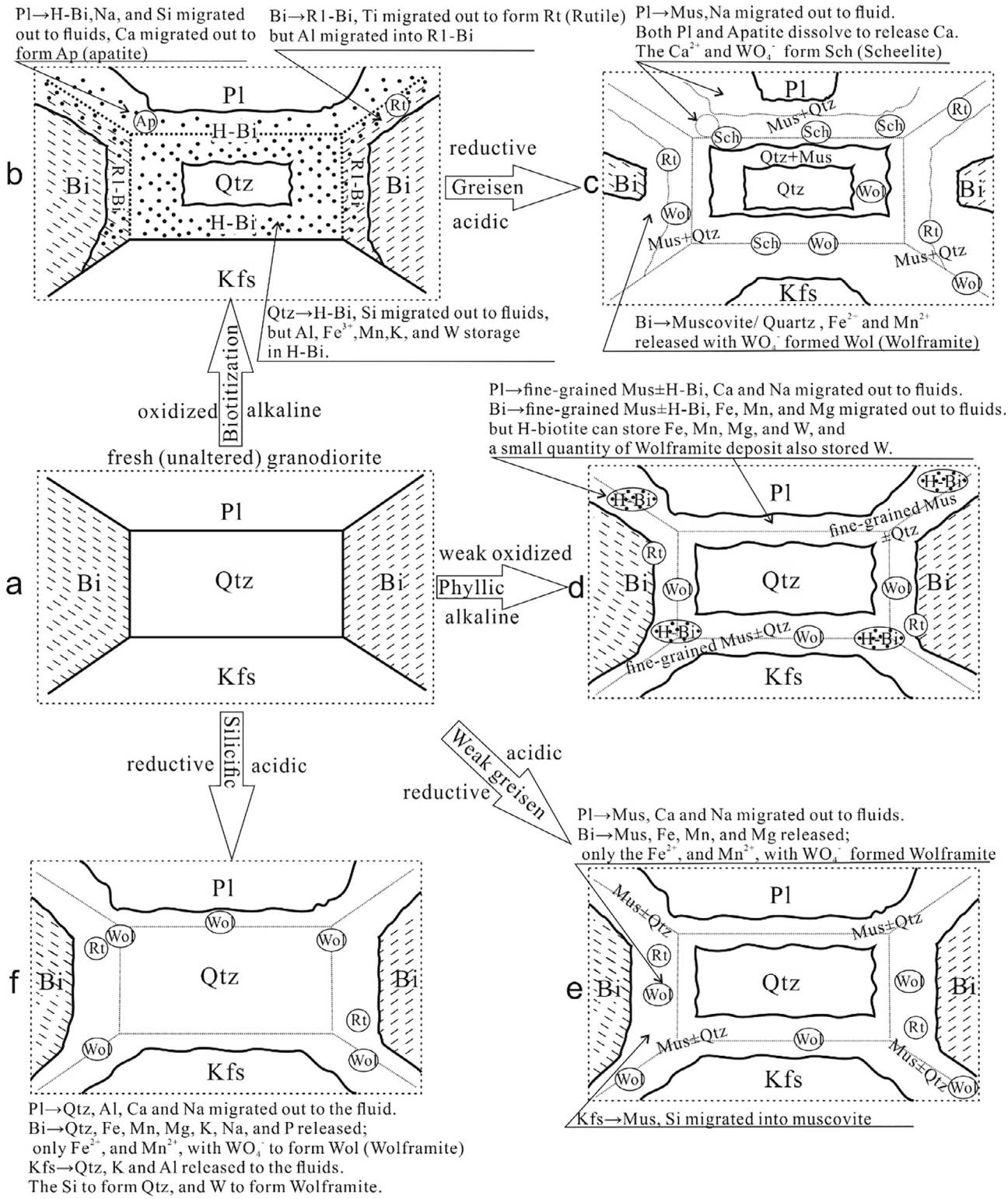

Fig. 9. Model of the migration of elements through fluid-solid (hydrothermal mineral crystals) interactions. Pl (plagioclase); Kfs (K-feldspar); Bi (biotite); H-Bi (hydrothermal biotite); R1-Bi (re-equilibrated biotite from the Jiuling granodiorite); Mus (muscovite); Ap apatite); Rt (rutile); Sch (scheelite); Wol (wolframite). (a) Unaltered granodiorite; (b) Biotitized granodiorite; (c) Biotitized + greisenized granodiorite; (d) Phyllic granodiorite; (e) Greisenic granodiorite; (f) Silicified granodiorite.

significant Ca for the formation of scheelite (Hu et al., 2004; Oliver et al., 2004; Parsons et al., 2009). Thus, different types of alteration would have various contributions for tungsten mineralization.

At Dahutang, the tungsten mineralization is associated with superimposed alteration (alkaline by acidic) (Fig. 2b). Different degrees of superposition resulted in variable tungsten mineralization. Calcium and Fe-Mn came from plagioclase and biotite, respectively, in the Jiuling (Neoproterozoic) biotite granodiorite (Table 2). They could not

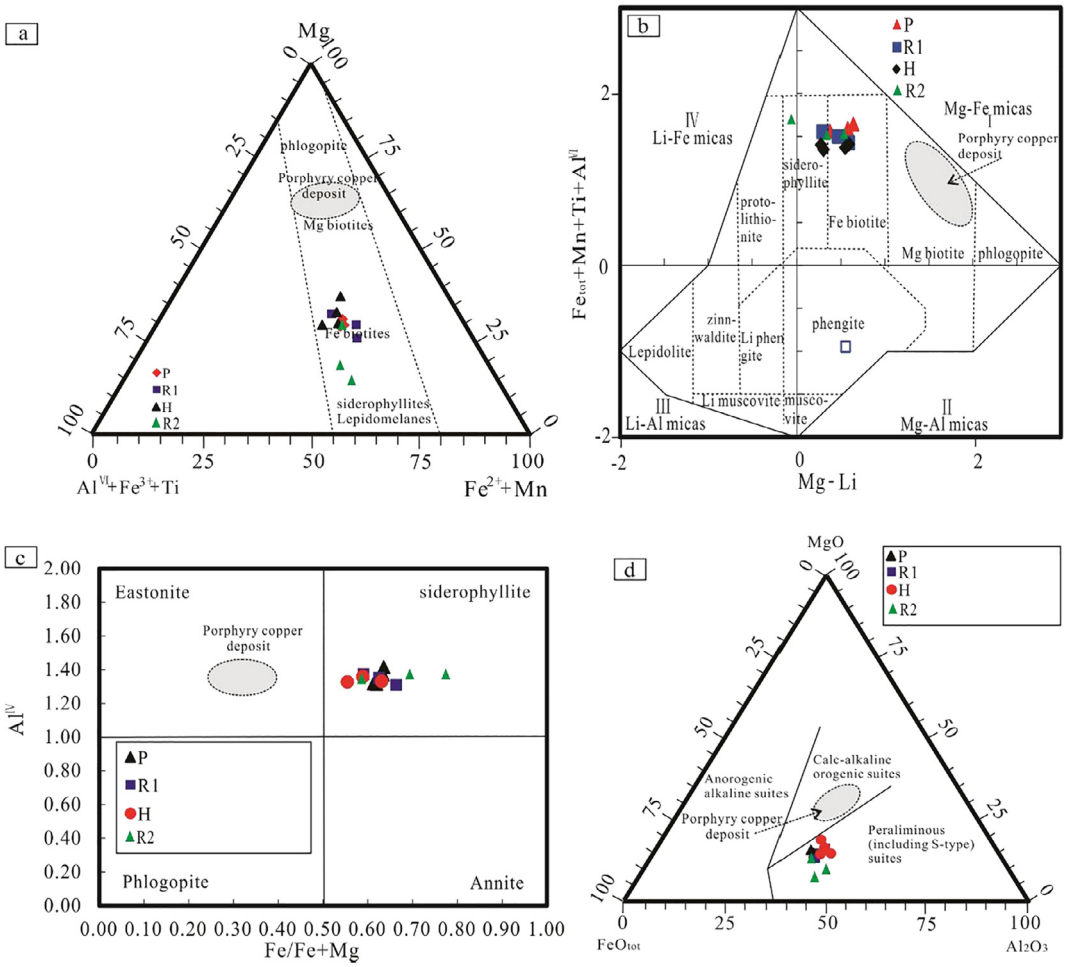

Fig. 10. Comparison of porphyry copper deposit system. P (Primary biotite); R1 (Re-equilibrated biotite from granodiorite); H (Hydrothermal biotite); R2 (Re-equilibrated biotite from porphyritic biotite granite). (a) Plot of biotite data from altered rocks in the Dahutang tungsten deposit on a ternary Mg–(Fe^{2+} + Mn)–(Al^{VI} + Fe^{3+} + Ti) diagram (Foster, 1960). (b) Chemical compositions of biotite on an (Mg–Li) vs. (Fe_{tot} + Mg + Ti–Al^{VI}) classification diagram (Tischendorf et al., 1997). (c) Plot of Fe/(Fe + Mg) vs. Al^{IV} in biotite from the Dahutang tungsten deposit (Deer et al., 1992). (d) Distribution of micas on a ternary MgO–FeO_{tot}–Al_2O_3 tectonomagmatic discrimination diagram (Abdelrahman, 1994). The porphyry copper deposit is from (Afshooni et al., 2013; Einali et al., 2014; Parsapoor et al., 2015).

be released into the hydrothermal fluid during biotite alteration (Fig. 7a). However, apatite and secondary biotite could be formed and act as large storage places for Ca and Fe-Mn, respectively. These minerals could be easily dissolved by acidic fluids so that Ca, Fe and Mn could be released into later hydrothermal fluids to form scheelite and wolframite in greisenized rock. During the superposition of alteration processes, ore-forming fluids contain a mass of Ca, Fe and Mn to form a tungsten deposit with similar scheelite and wolframite reserves (scheelite:wolframite ≈ 1:1).

This alteration and tungsten mineralization model for the Dahutang tungsten deposit can be summarized as in Fig. 11 in terms of the element behavior during variable alteration at the Dahutang tungsten deposit.

8. Conclusions

The Dahutang W deposit has at least five types of hydrothermal alteration, including biotite alteration, phyllic alteration, greisenization, silicification, and biotite alteration + greisenization.

The elements Ti, Ni, V, Sc, and Lu exhibited weak mobility (immobility) during all the alteration processes. The elements Al, Fe, Mn, Mg, K, P, and W migrated in, and Si, Ca, K and Na migrated out during the biotite alteration. Aluminum exhibited immobility during the phyllic alteration. The elements Si, Fe, K, P, and W migrated in, while Na, Mg, and Ca migrated out during the greisenization process. Aluminum and manganese exhibited immobility during the weak greisen alteration process. The elements Mg, Ca, Na and W exhibited moderate mobility; Mg, Ca, and Na moved out, while W moved into the altered rock during the silicification alteration process.

Three distinct hydrothermal fluids have been recognized. The first hydrothermal fluid caused alkaline (biotitization) alteration and Fe + Mn ± W mineralization at temperatures ranging from 450 to 560 °C; the second hydrothermal fluid was formed mainly by the mixing of magmatic fluid with a predominantly meteoric fluid at temperatures of 440–450 °C; the third hydrothermal fluid caused acidic (greisenization and silicification) alteration and W + Cu + Mo mineralization at temperatures ranging from 440 to 160 °C.

The superimposed alteration (alkaline followed by acidic) might be one of the most important reasons for the extensive tungsten ores at Dahutang. Biotite and apatite acted as storage places for Fe-Mn and Ca, respectively, during alkaline alteration, and these minerals subsequently decomposed during acidic alteration to form wolframite and scheelite.

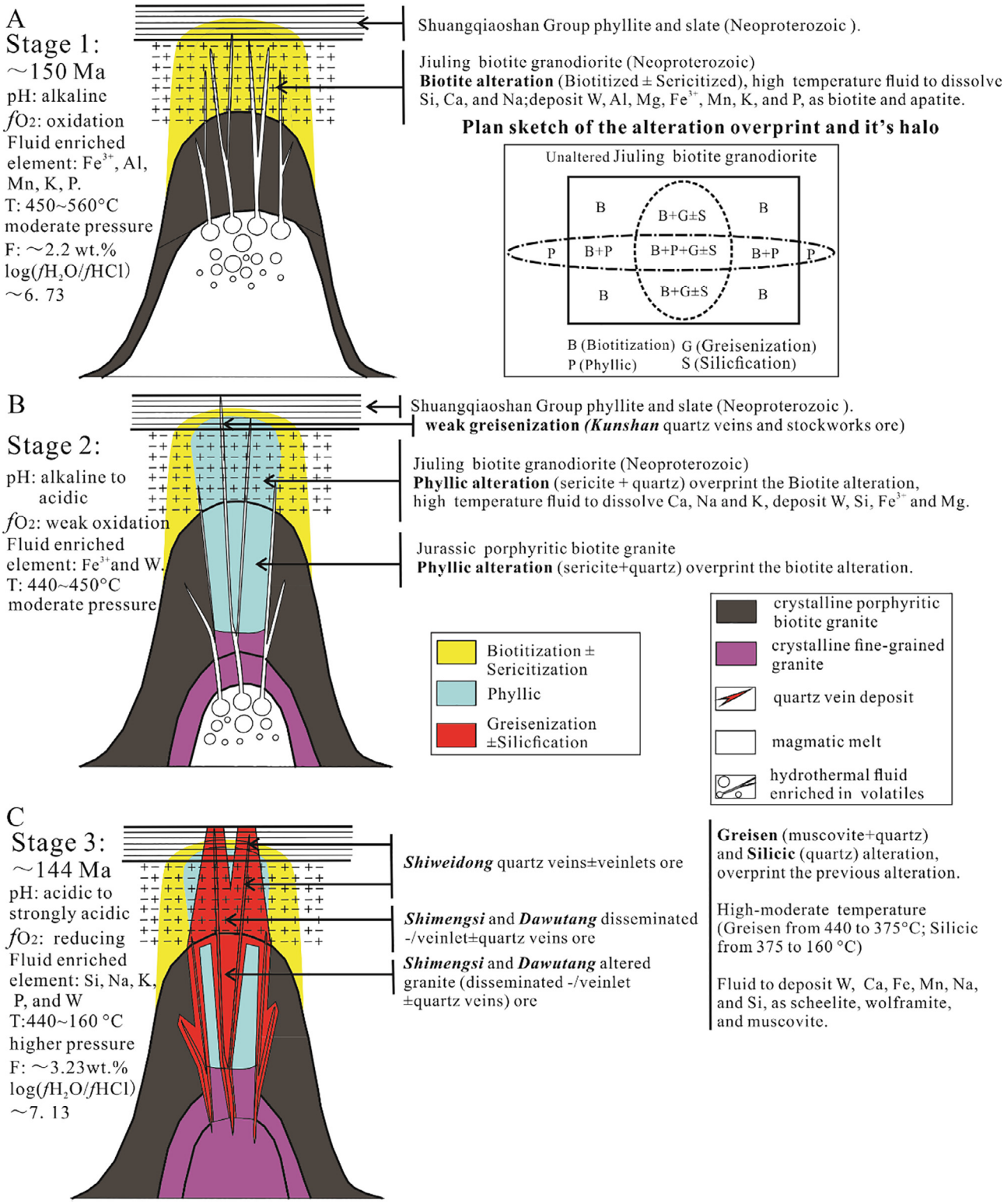

Fig. 11. Genetic model for the Dahutang tungsten deposit.

Acknowledgments

This research is jointly funded by the National key basic research and development program (973 Program) of China (no. 2014CB440904), Integrated exploration project of China Geological Survey (no. 12120114034501) and the "CAS Hundred Talents" Project to Jian-Feng Gao. We would like to thank Mr. Xiang Xinkui, Mr. Liu Nanqin and their co-workers from the Jiangxi Bureau of Geology, Mineral Resources, Exploration and Development, and its affiliated No. 916 Geological Team and Northwestern Geological Team, for field guidance and constructive discussions.

Appendix A. Supplementary data

Supplementary data associated with this article can be found, in the online version, at http://dx.doi.org/10.1016/j.oregeorev.2018.04.006.

References

Abdelrahman, A.M., 1994. Nature of biotite from alkaline, calc-alkaline, and peraluminous magmas. J. Petrol. 35, 525–541.

Afshooni, S.Z., Mirnejad, H., Esmaeily, D., Haroni, H.A., 2013. Mineral chemistry of hydrothermal biotite from the Kahang porphyry copper deposit (NE Isfahan), Central Province of Iran. Ore Geol. Rev. 54, 214–232.

Aliyari, F., Rastad, E., Goldfarb, R.J., Sharif, J.A., 2014. Geochemistry of hydrothermal alteration at the Qolqoleh gold deposit, northern Sanandaj-Sirjan metamorphic belt, northwestern Iran: vectors to high-grade ore bodies. J. Geochem. Explor. 140, 111–225.

Appel, P.W.U., 1994. Stratabound scheelite in altered Archaean komatiites. West Greenl. Mineralium Deposita. 29, 341–352.

Azadbakht Z., Lentz D.R., Mcfarlane C., 2014. Using biotite composition of the Devonian Lake George granodiorite, New Brunswick, as a case study for W-Mo-Au-Sb mineralized magmatic hydrothermal systems. Gac-Mac.

Barsukov, V.L., 1957. The geochemistry of tin. Geokimiya 1, 41–53.

Beran, A., Göd, R., Götzinger, M., Zemann, J., 1985. A scheelite mineralization in calc-silicate rocks of the Moldanubicum (Bohemian Massif) in Austria. Miner. Deposita 20, 16–22.

Chen, G.H., Wan, H.Z., Shu, L.S., 2012. An analysis on ore-controlling conditions and geological features of the Cu-W polymetallic ore deposit in the Zhuxi area of Jingdezhen, Jiangxi Province. Acta Petrol. Sin. 28, 3901–3914 (in Chinese with English abstract).

Chen, Y.W., Bi, X.W., Hu, R.Z., Zhu, W.G., Xu, L.L., Dong, S.H., 2010. The geochemical characteristics of biotites and their constraints on uranium mineralization in guidong pluton. Bull. Mineral. Petrol. Geochem. 29, 355–363 (in Chinese with English abstract).

Chu, Y., Lin, W., Faure, M., Wang, Q., 2015. Early Mesozoic intracontinental orogeny: example of the Xuefengshan-Jiuling Belt. Acta Petrol. Sin. 31, 2145–2155 (in Chinese with English abstract).

Cooke, D.R., Hollings, P., Wilkinson, J.J., Tosdal, R.M., 2014. 13.14–Geochemistry of porphyry deposits. Treatise on Geochem. 1, 357–381.

Corbett, G.J., Leach, T.M., 1998. Southwest Pacific Rim gold-copper systems: structure, alteration and mineralisation. Soc. Econ. Geol.

Deer, W.A., Howie, R.A., Zussman, J., 1992. An Introduction to the Rock-Forming Minerals. Longman Scientific & Technical.

Ding, X., Jiang, S.Y., Ni, P., Gu, L.X., Jiang, Y.H., 2005. Zircon SIMS U-Pb Geochronology of Host Granitoids in Wushan and Yongping Copper Deposits, Jiangxi Province. Geol. J. China Univ. 11, 383–389 (in Chinese with English abstract).

Douce, A.E.P., 1993. Titanium substitution in biotite: an empirical model with applications to thermometry, O_2 and H_2O barometries, and consequences for biotite stability. Chem. Geol. 108, 133–162.

Durand, C., Oliot, E., Marquer, D., Sizun, J.P., 2015. Chemical mass transfer in shear zones and metacarbonate xenoliths: a comparison of four mass balance approaches. Eur. J. Mineral. 27, 731–754.

Dymek, R.F., 1983. Titanium, aluminum and interlayer cation substitutions in biotite from high-grade gneisses. West Greenl. Am. Mineral. 68, 880–899.

Einali, M., Alirezaei, S., Zaccarini, F., 2014. Chemistry of magmatic and alteration minerals in the Chahfiruzeh porphyry copper deposit, south Iran: implications for the evolution of the magmas and physicochemical conditions of the ore fluids. Turkish J. Earth Sci. 23, 147–165.

Eugster, H.P., 1985. Granites and hydrothermal ore deposits: a geochemical framework. Mineral. Mag. 49, 7–23.

Feng, C.Y., Zeng, Z.L., Zhang, D.Q., Qu, W.J., Du, A.D., Li, D.X., She, H.Q., 2011. SHRIMP zircon U-Pb and molybdenite Re-Os isotopic dating of the tungsten deposits in the Tianmenshan-Hongtaoling W-Sn ore field, southern Jiangxi Province, China, and geological implications. Ore Geol. Rev. 43, 8–25.

Feng, C.Y., Zhang, D.Q., Xiang, X.K., Li, D.X., Qu, H.Y., Liu, J.N., Xiao, Y., 2012. Re-Os isotopic dating of molybdenite from the Dahutang tungsten deposit in northwestern Jiangxi Province and its geological implication. Acta Geol. Sin. 28, 3858–3868 (in Chinese with English abstract).

Foster, M.D., 1960. In: Interpretation of the Composition of Trioctahedral Micas. United States government printing office, Washington, pp. 1–49.

Gao, J.-F., Lu, J.-J., Lai, M.-Y., Lin, Y.-P., Pu, W., 2003. Analysis of trace elements in rock samples using HR-ICPMS. J. Nanjing Univ. 39, 844–850 (in Chinese with English abstract).

Gao, L.Z., Chen, J., Ding, X.Z., Liu, Y.R., Zhang, C.H., Zhang, H., Liu, Y.X., Pang, W.H., Zhang, Y.H., 2011. Zircon SHRIMP U-Pb dating of the tuff bed of Lengjiaxi and Banxi groups, northeastern Hunan: Constraints on the Wuling Movement. Geol. Bull. China 30, 1001–1008 (in Chinese with English abstract).

Gao, L.Z., Chen, J.S., Dai, C.G., Ding, X.Z., Wang, X.H., Liu, Y.X., Wang, M., Zhang, H., 2014. SHRIMP zircon U-Pb dating of tuff in Fanjingshan Group and Xiajiang Group from Guizhou and Hunan Provinces and its stratigraphic implications. Geol. Bull. China. 33, 949–959 (in Chinese with English abstract).

Gao, L.Z., Dai, C.G., Liu, Y.X., Wang, M., Wang, X.H., Chen, J.S., Ding, X.Z., Zhang, C.H., Cao, Q., Liu, J.H., 2010. Zircon SHRIMP U-Pb dating of tuff bed of the Sibao Group in southeastern Guizhou-northern Guangxi area, China and its stratigraphic implication. Geol. Bull. China 29, 1259–1267 (in Chinese with English abstract).

Gao, L.Z., Ding, X.Z., Zhang, C.H., Chen, J., Liu, Y.R., Zhang, H., Liu, X.X., Pang, W.H., 2012a. Revised Chronostratigraphic Framework of the Metamorphic Strata in the Jiangnan Orogenic Belt, South China and its Tectonic Implications. Acta Geol. Sin. (English Edition) 86, 339–349.

Gao, L.Z., Huang, Z.Z., Ding, X.Z., Liu, Y.X., Zhang, C.H., Wang, Z.Q., Pang, J.F., Han, K.Y., 2012b. The Geochronological Relationship between the Shaojiwa Formation and the Xingzi Complex Group inNorthwestern Jiangxi and the Constraints on Zircon SHRIMP U-Pb Age. Acta Geoscientica Sin. 33, 295–304 (in Chinese with English abstract).

Gao, L.Z., Yang, M.G., Ding, X.Z., Liu, Y.X., Liu, X., Ling, L.H., Chuan, H.Z., 2008. SHRIMP U-Pb zircon dating of tuff in the Shuangqiaoshan and Heshangzhen groups in South China-constraints on the evolution of the Jiangnan Neoproterozoic orogenic belt. Geol. Bull. China 27, 1744–1751 (in Chinese with English abstract).

Grant, J.A., 1986. The isocon diagram-a simple solution to Gresens' equation for Metasomatic alteration. Econ. Geol. 81, 1976–1982.

Gresens, R.L., 1967. Composition-volume relationships of metasomatism. Chem. Geol. 2, 47–65.

Guan, J.P., He, B., Li, D.W., 2010. SIMS U-Pb Dating of the Detrital Zircons From the Xingzi Group in Lushan Area and Its Geological Significance. Geotectonica Et Metallogenia 34, 402–407 (in Chinese with English abstract).

Gustafson, L.B., Hunt, J.P., 1975. The porphyry copper deposit at El Salvador, Chile. Econ Geol 70: 857–912. Econ. Geol. 70, 857–912.

Han, L., Huang, X., Li, J., He, P., Yao, J., 2016. Oxygen fugacity variation recorded in apatite of the granite in the Dahutang tungsten deposit, Jiangxi Province, South China. Acta Petrol. Sin. 32, 746–758 (in Chinese with English abstract).

Han, Y., Zhang, C.H., Liu, Z.H., You, G.Q., Li, L.Y., 2015. Study on Sedimentary Characteristics, Detrital Zircon Ages and Tectono-Paleogeographic Setting of Neoproterozoic Pingshui Group in Pujiang Area, Zhejiang Province. Geol. Review. 61, 1270–1280 (in Chinese with English abstract).

Harris, A.C., Golding, S.D., 2002. New evidence of magmatic-fluid related phyllic alteration: Implications for the genesis of porphyry Cu deposits. Geology 30, 335–338.

Heinrich, C.A., Candela, P.A., 2014. 13.1-Fluids and Ore Formation in the Earth's Crust. Treatise on Geochem. 3, 1–28.

Henry, D.J., 2005. The Ti-saturation surface for low-to-medium pressure metapelitic biotites: implications for geothermometry and Ti-substitution mechanisms: american Mineralogist. Am. Mineral. 90, 316–328.

Hu, S.X., Ye, Y., Fang, C.Q., 2004. In: Petrology of Metasomatic Rocks and Implieations Fur Ore Exploration. Geological publishing house, Beijing, pp. 109 (in Chinese).

Hu, Z.H., Liu, D., Liu, S.B., Lang, X.H., Zhang, J.J., Chen, Y.C., Shi, G.H., Wang, Y.Y., Lei, T.H., Nei, L.M., Sha, M., Gong, L.X., Liu, Z.Q., 2015. Rock-forming and ore-forming ages and significance of Taqian Mo(W)deposit, Leping, Jiangxi, China. J. Chengdu Univ. Technol. 42, 312–322 (in Chinese with English abstract).

Huang, L.C., Jiang, S.Y., 2013. Geochronology, geochemistry and petrogenesis of the tungsten-bearing porphyritic granite in the Dahutang tungsten deposit, Jiangxi Province. Acta Petrol. Sin. 29, 4323–4335 (in Chinese with English abstract).

Huang, L.C., Jiang, S.Y., 2014. Highly fractionated S-type granites from the giant Dahutang tungsten deposit in Jiangnan Orogen, Southeast China: Geochronology, petrogenesis and their relationship with W-mineralization. Lithos 202, 207–226.

Jia, L.Q., Xu, W.Y., Yang, D., Yang, Z.S., Wang, L., 2015a. Zircon U-Pb and molybdenite Re-Os dating of Baoshan porphyry Cu polymetallic deposit in Jiujiang-Ruichang ore concentration area of Jiangxi Province and its geological significance. Miner. Deposits 34, 63–68 (in Chinese with English abstract).

Jia, L.Q., Xu, W.Y., Yang, D., Yang, Z.S., Mo, X.X., Wang, L., 2015b. Zircon U-Pb and Molybdenite Re-Os Dating of the Dongleiwan Skarn Cu Polymetallic Deposit in Jiangxi Province, , Eastern China. Acta Geol. Sin. 36, 177–186 (in Chinese with English abstract).

Jiang, C.Q., 2016. In: The Research on the Geochemical Characteristic and Genesis of the Dawutang Tungsten Polymetallic Deposit in Jiangxi. East China University of Technology, Nanchang, pp. 64 (in Chinese with English abstract).

Jiang, S.Y., Peng, N.J., Huang, L.C., Xu, Y.M., Zhan, G.L., Dan, X.H., 2015. Geological characteristic and ore genesis of the giant tungsten deposits from the Dahutang ore-concentrated district in northern Jiangxi Province. Acta Petrol. Sin. 31, 639–655 (in Chinese with English abstract).

Klammer, D., 1997. Mass change during extreme acid-sulphate hydrothermal alteration of a Tertiary latite, Styria, Austria. Chem. Geol. 141, 33–48.

Kusakabe, M., 1984. Oxygen and sulfur isotopic compositions of quartz, anhydrite and sulfide minerals from the El Teniente and Rio Blanco porphyry copper deposits, Chile. Bull. Geol. Surv. Jap. 35, 583–614.

Kusakabe, M., Hori, M., Matsuhisa, Y., 1990. Primary mineralization-alteration of the El Teniente and Río Blanco porphyry copper deposits, Chile: Stable isotope, fluid inclusion and $Mg^{+2}/Fe^{+2}/Fe^{+3}$ ratios of hydrothermal fluids. In: Herbert, H.K., Ho, S.E. (Eds.), Stable isotopes and fluid processes in mineralization. University of Western Australia Press, Perth, pp. 244–259.

López-Moro, F.J., 2012. EASYGRESGRANT-A Microsoft Excel spreadsheet to quantify volume changes and to perform mass-balance modeling in metasomatic systems. Comput. Geosci. 39, 191–196.

Lentz, D., 1992. Petrogenesis and geochemical composition of biotites in rare-element granitic pegmatites in the southwestern Grenville Province, Canada. Mineral. Petrol. 46, 239–256.

Li, J., Huang, X.L., He, P.L., Li, W.X., Yu, Y., Chen, L.L., 2015. In situ analyses of micas in the Yashan granite, South China: Constraints on magmatic and hydrothermal evolutions of W and Ta–Nb bearing granites. Ore Geol. Rev. 65, 793–810.

Li, X.C., Fan, H.R., Santosh, M., Hu, F.F., Yang, K.F., Lan, T.G., 2013. Hydrothermal alteration associated with Mesozoic granite-hosted gold mineralization at the Sanshandao deposit, Jiaodong Gold Province, China. Ore Geol. Rev. 53, 403–421.

Li, X.H., Li, W.X., Li, Z.X., Lo, C.H., Wang, J., Ye, M.F., Yang, Y.H., 2009. Amalgamation

between the Yangtze and Cathaysia Blocks in South China: Constraints from SHRIMP U-Pb zircon ages, geochemistry and Nd–Hf isotopes of the Shuangxiwu volcanic rocks. Precambr. Res. 174, 117–128.
Li, X.H., Li, Z.X., Ge, W., Zhou, H., Li, W., Liu, Y., Wingate, M.T.D., 2003. Neoproterozoic granitoids in South China: crustal melting above a mantle plume at ca. 825 Ma? Precambr. Res. 122, 45–83.
Li, Y., Pan, X.F., Zhao, M., Chen, G.H., Zhang, T.F., Liu, X., Zhang, C., 2014. LA-ICP-MS Zircon U-Pb Age, Geochemical Features and Relations to the W-Cu Mineralization of Granitic Porphyry in Zhuxi Skarn Deposit, Jingdezhen, Jiangxi. Geol. Review. 60, 693–708 (in Chinese with English abstract).
Liang, Q., Grégoire, D.C., 2000. Determination of Trace Elements in Twenty Six Chinese Geochemistry Reference Materials by Inductively Coupled Plasma-Mass Spectrometry. Geostand. Geoanal. Res. 24, 51–63.
Liu, J., Mao, J., Ye, H., Zhang, W., 2011. Geology, geochemistry and age of the Hukeng tungsten deposit, Southern China. Ore Geol. Rev. 43, 50–61.
Liu, J., Mao, J.W., Ye, H.S., Xie, G.Q., Yang, G.Q., Zhang, W., 2008. Zircon LA-ICPMS U-Pb dating of Hukeng granite in Wugongshan area, Jiangxi Province and its geoehemical characteristics. Acta Petrol. Sin. 24, 1813–1822 (in Chinese with English abstract).
Liu, S.B., Liu, Z.Q., Wang, C.H., Wang, D.H., Zhao, Z., Hu, Z.H., 2017. Geochemical characteristics of REEs and trace elements and Sm-Nd dating of scheelite from the Zhuxi giant tungsten deposit in northeast Jiangxi. Earth Sci. Front. 24, 17–30 (in Chinese with English abstract).
Liu, Y.J., Ma, D.S., 1987. In: Geochemistry of Tungsten. Science Press, Beijing, pp. 232 (in Chinese).
Liu, Y.Y., Ma, C.Q., Zhao, Y., Huang, W.P., 2012. Zircon U-Pb age, element and Sr-Nd-Hf isotope geochemistry of Late Mesozoic magmatism from the Guichi metallogenic district in the Middle and Lower Reaches of the Yangtze River Region. Acta Petrol. Sin. 28, 3287–3305 (in Chinese with English abstract).
Lou, F.S., Shen, W.Z., Wang, D.Z., Shu, L.S., Wu, F.J., Zhang, F.R., Yu, J.H., 2005. Zircon U-Pb Isotopic Chronology of the Wugongshan Dome Compound Granite in Jiangxi Province. Acta Geol. Sin. 79, 637–644 (in Chinese with English abstract).
Lowell, J.D., Guilbert, J.M., 1970. Lateral and vertical alteration-mineralization zoning in porphyry ore deposits. Econ. Geol. 65, 373–408.
Luo, L., Jiang, S., Yang, S., Zhao, K., Wang, S., Gao, W., 2010. Petrochemistry, zircon U-Pb dating and Hf isotopic composition of the granitic pluton in the Pengshan Sn-polymetallic orefield, Jiangxi Province. Acta Petrol. Sin. 26, 2818–2834 (in Chinese with English abstract).
Maclean, W.H., 1988. Rare earth element mobility at constant inter-REE ratios in the alteration zone at the Phelps Dodge massive sulphide deposit, Matagami, Quebec. Mineralium Deposita 23, 231–238.
Maclean, W.H., 1990. Mass change calculations in altered rock series. Miner. Deposita 25, 44–49.
Maclean, W.H., Kranidiotis, P., Maclean, W.H., Kranidiotis, P., 1987. Immobile elements as monitors of mass transfers in hydrothermal alteration: Phelps Dodge massive sulfide deposit, Matagami, Quebec. Econ Geol. Economic Geol. 82, 951–962.
Mao, J.W., Guy, B., Raimbault, L., Shimazaki, H., 1996. Manganese Skarn in the Shizhuyuan Polymetallic Tungsten Deposit, Hunan. China. Resource Geology. 46, 1–11.
Mao, Z.H., Cheng, Y.B., Liu, J.J., Yuan, S.D., Wu, S.H., Xiang, X.K., Luo, X.H., 2013. Geology and molybdenite Re–Os age of the Dahutang granite-related veinlets-disseminated tungsten ore field in the Jiangxin Province. China. Ore Geology Reviews. 53, 422–433.
Mao, Z.H., Liu, J.J., Mao, J.W., Deng, J., Zhang, F., Meng, X.Y., Xiong, B.K., Xiang, X.K., Luo, X.H., 2015. Geochronology and geochemistry of granitoids related to the giant Dahutang tungsten deposit, middle Yangtze River region, China: Implications for petrogenesis, geodynamic setting, and mineralization. Gondwana Res. 28, 816–836.
Meng, Q.X., Jian, Z., Geng, J.Z., Zhang, C.L., Huang, W.C., 2013. Zircon U-Pb age and Hf isotope compositions of Lengjiaxi and Baxi Groups in middle Hunan Province: implications for the Neoproterozoic tectonic evolution in South China. Geology in China. 40, 191–216 (in Chinese with English abstract).
Moore, W.J., Czamanske, G.K., 1973. Compositions of biotites from unaltered and altered monzonitic rocks in the Bingham Mining District. Utah. Econ. Geol. 68, 269–274.
Munoz, J.L., 1984. F-OH and Cl-OH exchange in micas with applications to hydrothermal ore deposits. Rev. Mineral. Geochem. 13 (1), 469–493.
Munoz, J.L., 1992. Calculation of HF and HCl fugacities from biotite compositions: revised equations. Geol. Soc. Am., Abstr. Programs 24, A221.
Neinavaie, H., Thalmann, F., Ataii, B., Beran, A., 1989. Wolframite- and scheelite-bearing carbonate rocks of the Nock mountains, Austria: A new type of tungsten mineralization in the Eastern Alps. Miner. Deposita 24, 14–18.
Neves, L.J.P.F., 1997. Trace element content and partitioning between biotite and muscovite of granitic rocks: A study in the Viseu region (Central Portugal). Eur. J. Mineral. 9, 849–857.
Oliver, N.H.S., Cleverley, J.S., Mark, G., Pollard, P.J., Fu, B., Marshall, L.J., Rubenach, M.J., Williams, P.J., Baker, T., 2004. Modeling the Role of Sodic Alteration in the Genesis of Iron Oxide-Copper-Gold Deposits, Eastern Mount Isa Block, Australia. Econ. Geol. 99, 1145–1176.
Parsapoor, A., Khalili, M., Tepley, F., Maghami, M., 2015. Mineral chemistry and isotopic composition of magmatic, re-equilibrated and hydrothermal biotites from Darreh-Zar porphyry copper deposit, Kerman (Southeast of Iran). Ore Geol. Rev. 66, 200–218.
Parsons, I., Magee, C.W., Allen, C.M., Shelley, J.M.G., Lee, M.R., 2009. Mutual replacement reactions in alkali feldspars II: trace element partitioning and geothermometry. Contrib. Miner. Petrol. 157, 663–687.
Pirajno, F., 1982. Geology, geochemistry, mineralisation, and metal zoning of the McConnochie greisenised granite, Reefton district, Westland, New Zealand. N. Z. J. Geol. Geophys. 25, 405–425.
Pirajno, F., 2009. Hydrothermal Processes and Wall Rock Alteration. Hydrothermal Processes and Mineral Systems. Springer Netherlands, Dordrecht, pp. 73–164.
Pirajno, F., 2013. Chapter 7 Effects of Metasomatism on Mineral Systems and Their Host Rocks: Alkali Metasomatism, Skarns, Greisens, Tourmalinites, Rodingites, Black-Wall Alteration and Listvenites. Metasomatism and the Chemical Transformation of Rock. Springer Berlin Heidelberg, pp. 203–251.
Pirajno, F., 2013b. In: Yangtze Craton, Cathaysia and the South China Block. The Geology and Tectonic Settings of China's Mineral Deposits. Springer Netherlands, Dordrecht, pp. 127–247.
Plimer, I.R., 1994. Strata-bound scheelite in meta-evaporites, Broken Hill, Australia. Econ. Geol. 89, 423–437.
Putnis, A., 2009. Mineral replacement reactions. Rev. Mineral. Geochem. 70, 87–124.
Raith, J.G., 1991. Stratabound tungsten mineralization in regional metamorphic calc-silicate rocks from the Austroalpine Crystalline Complex, Austria. Mineralium Deposita. 26, 72–80.
Raith, J.G., Prochaska, W., 1995. Tungsten Deposits in the Wolfram Schist, Namaqualand, South Africa: Strata-Bound Versus Granite-Related Genetic Concepts. Econ. Geol. 90, 1934–1954.
Raith, J.G., Stein, H.J., 2000. Re-Os dating and sulfur isotope composition of molybdenite from tungsten deposits in western Namaqualand, South Africa: implications for ore genesis and the timing of metamorphism. Miner. Deposita 35, 741–753.
Ruan, K., Pan, J.Y., Wu, J.Y., Xiang, X.K., Liu, W.Q., Li, Z.S., 2015. Geochemical characteristics and ore genesis of the shimensi cryptoexplosive breccia type tungsten deposit in dahutang, Jiangxi Province. Bull. Mineral. Petrol. Geochem. 34, 633–641 (in Chinese with English abstract).
Selby, D., Nesbitt, B.E., 2000. Chemical composition of biotite from the Casino porphyry Cu-Au-Mo mineralization, Yukon, Canada: evaluation of magmatic and hydrothermal fluid chemistry. Chem. Geol. 171, 77–93.
Shcherba, G.N., 1970. Greisens. Int. Geol. Rev. 12, 114–150.
Shu, L.S., 2012. An analysis of principal features of tectonic evolution in South China Block. Geol. Bull. China 31, 1035–1053 (in Chinese with English abstract).
Shu, L.S., Shi, Y.S., Guo, L.Z., 1995. In: The Late Proterozoic Plate Tectonics and Collisional Kinematics in the Middle Part of the Jiangnan Belt. Nanjing University Publishing House, Nanjing, pp. 174 (in Chinese).
Sillitoe, R.H., 1997. Characteristics and controls of the largest porphyry copper-gold and epithermal gold deposits in the circum-Pacific region. Aust. J. Earth Sci. 44, 373–388.
Sillitoe, R.H., 2010. Porphyry copper systems. Econ. Geol. 105, 3–41.
Soloviev, S.G., Kryazhev, S., 2016. Geology, mineralization, and fluid inclusion characteristics of the Chorukh-Dairon W-Mo-Cu skarn deposit in the Middle Tien Shan, Northern Tajikistan. Ore Geol. Rev. 80, 79–102.
Taylor R.G., 1979. Geology of tin deposits: Elsevier Scientific Pub. Co., distributors for the U.S. and Canada, Elsevier/North-Holland.
Thalhammer, O.A.R., Stumpfl, E.F., Jahoda, R., 1989. The Mittersill scheelite deposit, Austria. Econ. Geol. 84, 1153–1571.
Tindle, A.G., Webb, P.C., Tindle, A.G., 1995. Estimation of lithium contents in trioctahedral micas using microprobe data; application to micas from granitic rocks. Chemom. Intell. Lab. Syst. 29, 148–149.
Tischendorf, G., Foerster, H.J., Gottesmann, B., 1999. The correlation between lithium and magnesium in trioctahedral micas: Improved equations for Li_2O estimation from MgO data. Mineral. Mag. 63, 57–74.
Tischendorf, G., Gottesmann, B., Förster, H.J., Trumbull, R.D., 1997. On Li-bearing micas: estimating Li from electron microprobe analyses and an improved diagram for graphical representation. Mineral. Mag. 61, 809–834.
Uchida, E., Endo, S., Makino, M., 2007. Relationship between solidification depth of granitic rocks and formation of hydrothermal ore deposits. Resour. Geol. 57, 47–56.
Wang, H., Feng, C., Zhao, Y., Zhang, M., Chen, R., Chen, J., 2016. Ore genesis of the lunwei granite-related scheelite deposit in the wuyi metallogenic belt, southeast china: constraints from geochronology, fluid inclusions, and H-O–S isotopes. Resour. Geol. 66, 240–258.
Wang, Q., Zhao, Z.H., Jian, P., Xu, J.F., Bao, Z.W., Ma, J.L., 2004. SHRIMP zircon geochronology and Nd-Sr isotopic eochemistry of the Dexing granodiorite porphyries. Acta Petrol. Sin. 20, 315–324 (in Chinese with English abstract).
Wang, X.L., Shu, L.S., Xing, G.F., Zhou, J.C., Tang, M., Shu, X.J., Qi, L., Hu, Y.H., 2012. Post-orogenic extension in the eastern part of the Jiangnan orogen: Evidence from ca 800–760Ma volcanic rocks. Precambr. Res. 222–223, 404–423.
Wang, X.L., Zhao, G.C., Zhou, J.C., Liu, Y.S., Hu, J., 2008. Geochronology and Hf isotopes of zircon from volcanic rocks of the Shuangqiaoshan Group, South China: Implications for the Neoproterozoic tectonic evolution of the eastern Jiangnan orogen. Gondwana Res. 14, 355–367.
Wang, X.L., Zhou, J.C., Griffin, W.L., Wang, R.C., Qiu, J.S., O'Reilly, S.Y., Xu, X.S., Liu, X.M., Zhang, G.L., 2007. Detrital zircon geochronology of Precambrian basement sequences in the Jiangnan orogen: Dating the assembly of the Yangtze and Cathaysia Blocks. Precambr. Res. 159, 117–131.
Watanabe, Y., Hedenquist, J.W., 2001. Mineralogical and stable isotope zonation at the surface over the El Salvador porphyry Cu deposit, Chile. Econ. Geol. 96, 1775–1797.
Wei, W.F., Yan, B., Shen, N.P., Liu, L., Zhang, Y., Xiang, X.K., 2017. Muscovite 40Ar/39Ar Age and H-O-S Isotopes of the Shimensi Tungsten Deposit (Northern Jiangxi Province, South China) and Their Metallogenic Implications. Minerals 7, 162.
Wolfe, R., Cooke, D., Hooper, B., Heithersay, P., 1996. A magmatic origin for late-stage sericite-alunite alteration at the Endeavour 48 Cu-Au porphyry deposit, Goonumbla, NSW, 13th Australian Geological Convention, Canberra. Earth Sciences, Australia, pp. 480.
Wones, D.R., Eugster, H.P., 1965. Stability of biotite: experiment, theory, and application. Am. Mineral. 50, 1228–1272.
Xiang, X.K., Chen, M.S., Zhan, G.N., Qian, Z.Y., Li, H., Xu, J.H., 2012. Metallogenic geological conditions of Shimensi tungsten-polymetallic deposit in north Jiangxi

province. Contributions to Geology & Mineral Resources Research. 27, 143–155 (in Chinese with English abstract).
Xiang, X.K., Wang, P., Sun, D.M., Zhong, B., 2013. Re-Os isotopic age of molybdeinte from the Shimensi tungsten polymetallic deposit in northern Jiangxi province and its geological implications. Geol. Bull. China. 32, 1824–1831 (in Chinese with English abstract).
Xiong, X., Xu, W.Y., Wen, C.H., 2015. Fluid characteristics and genesis of Xianglushan skam scheelite deposit in. Mineral Deposits 34, 1046–1056 (in Chinese with English abstract).
Xu, G.H., 2013. In: The geochemical characteristics and metallogenic mechanism of Shiweidong Tungsten deposit, North Jiangxi Province. East China University of Technology, Nanchang, pp. 57 (in Chinese with English abstract).
Xu, X.B., Tang, S., Li, Y., Zhang, Z.J., 2015. Characteristics of Neoproterozoic-Early Mesozoic multiphase orogenic activities of Eastern Jiangnan Orogen. Geol. China 42, 33–50 (in Chinese with English abstract).
Xu, X.B., Zhang, Y.Q., Jia, D., Shu, L.S., Wang, R.R., 2009. Early Mesozoic geotectonic processes in South China. Geol. China 36, 573–593 (in Chinese with English abstract).
Yang, M.G., Wang, F.N., Zeng, Y., Lai, X.P., Huang, S.B., Zhou, H., 2004. In: Geology of Metallogenesis in Notherm Jiangxi Province. China Earth Press, Wuhan, pp. 186 (in Chinese).
Yang, P., Rivers, T., 2000. Trace element partitioning between coexisting biotite and muscovite from metamorphic rocks, Western Labrador: structural, compositional and thermal controls. Geochimica Et Cosmochimica Acta 64, 1451–1472.
Yavuz, F., 2003. Evaluating micas in petrologic and metallogenic aspect: I–definitions and structure of the computer program MICA^{+}. Comput. Geosci. 29, 1203–1213.
Ye, H.M., Zhang, X., Zhu, Y.H., 2016. In-situ monazite U-Pb geochronology of granites in Shimensi tungsten polymetallic deposit, Jiangxi Province and its geological significance. Geotectonica Et Metallogenia 40, 58–70 (in Chinese with English abstract).
Zaw, K., Peters, S.G., Cromie, P., Burrett, C., Hou, Z., 2007. Nature, diversity of deposit types and metallogenic relations of South China. Ore Geol. Rev. 31, 3–47.
Zhang, F.X., Pointeau, V., Shuller, L.C., Reaman, D.M., Lang, M., Liu, Z., Hu, J., Panero, W.R., Becker, U., Poinssot, C., Ewing, R.C., 2009. Structural transitions and electron transfer in coffinite, USiO4, at high pressure. Am. Mineral. 94, 916–920.
Zhang, M.Y., Feng, C.Y., Li, D.X., Wang, H., Zhou, J.H., Ye, S.Z., Wang, G.H., 2016. Geochronological study of the Kunshan W-Mo-Cu deposit in the Dahutang area, northern Jiangxi Province and its geological significance. Geotectonica Et Metallogenia 40, 503–516 (in Chinese with English abstract).
Zhang, W.W., 2013. In: The Inclusion Characteristics and Its Geological Siganificances of Dalingshang Tungsten Ore in Wuning, Jiangxi. East China University of Technology, Nanchang, pp. 69 (in Chinese with English abstract).
Zhang, Y., Pan, J.Y., Ma, D.S., Dan, X.H., Zhang, L.L., Xu, G.H., Yang, C.P., Jiang, Q.X., Jiang, C.Q., 2017. Re-Os molybdenite age of Dawutang tungsten ore district of northwest Jiangxi and its geological significance. Mineral Deposits 36, 749–769 (in Chinese with English abstract).
Zhang, Y.Q., Dong, S.W., Li, J.H., Cui, J.J., Shi, W., Su, J.B., Li, Y., 2012. The new progress in the study of Mesozoic tectonics of South China. Acta Geoscientica Sin. 33, 257–279 (in Chinese with English abstract).
Zhao, J.H., Zhou, M.F., Yan, D.P., Zheng, J.P., Li, J.W., 2011. Reappraisal of the ages of Neoproterozoic strata in South China: No connection with the Grenvillian orogeny. Geology 39, 299–302.
Zhao, W.W., Zhou, M.F., 2018. Mineralogical and metasomatic evolution of the Jurassic Baoshan scheelite skarn deposit, Nanling, South China. Ore Geol. Rev. 95, 182–194.
Zhao, W.W., Zhou, M.F., Li, Y.H.M., Zhao, Z., Gao, J.F., 2017. Genetic types, mineralization styles, and geodynamic settings of Mesozoic tungsten deposits in South China. J. Asian Earth Sci. 137, 109–140.
Zhao, Z., Zhao, W.W., Lu, L., Wang, H.Y., 2018. Constraints of multiple dating of the Qingshan tungsten deposit on the Triassic W(-Sn) mineralization in the Nanling region, South China. Ore Geol. Rev. 94, 46–57.
Zhong, Y.F., Ma, C.Q., She, Z.B., Lin, G.C., Xu, H.J., Wang, R.J., Yang, K.G., Liu, Q., 2005. SHRIMP U-Pb Zircon Geochronology of the Jiuling Granitic Complex Batholith in Jiangxi Province. Earth. Sci. J. China Univ. Geosci. 30, 685–691 (in Chinese with English abstract).
Zhou, M.F., Yan, D.P., Kennedy, A.K., Li, Y., Ding, J., 2002. SHRIMP U-Pb zircon geochronological and geochemical evidence for Neoproterozoic arc-magmatism along the western margin of the Yangtze Block, South China. Earth Planet. Sci. Lett. 196, 51–67.
Zhou, X.H., Zhang, Y.J., Liao, S.B., Yu, M.G., Chen, Z.H., Zhao, X.L., Yang, J., Jiang, R., 2012. LA-ICP-MS Zircon U-Pb Geochronology of Volcanic Rocks in the Shuangqiaoshan Group at Anhui-Jiangxi Boundary Region and Its Geological Implication. Geol. J. China Univ. 18, 609–622 (in Chinese with English abstract).
Zhu, C., Sverjensky, D.A., 1992. F-Cl-OH partitioning between biotite and apatite. Geochim. Cosmochim. Acta 56, 3435–3467.